NIH Public Access
Author Manuscript
Surf Sci Rep. Author manuscript; available in PMC 2015 September 01.

Published in final edited form as:
Surf Sci Rep. 2014 ; 69(2-3): 132–158. doi:10.1016/j.surfrep.2014.07.001.

Synthesis and surface functionalization of silica nanoparticles for nanomedicine

Alexander Liberman[a], **Natalie Mendez**[a], **William C. Trogler**[b], and **Andrew C. Kummel**[b,*]

[a]Materials Science and Engineering Program, University of California San Diego, 9500 Oilman Drive, La Jolla, CA 92093-0358, USA

[b]Department of Chemistry and Biochemistry, University of California San Diego, 9500 Oilman Drive, La Jolla, CA 92093-0358, USA

Abstract

There are a wide variety of silica nanoformulations being investigated for biomedical applications. Silica nanoparticles can be produced using a wide variety of synthetic techniques with precise control over their physical and chemical characteristics. Inorganic nanoformulations are often criticized or neglected for their poor tolerance; however, extensive studies into silica nanoparticle biodistributions and toxicology have shown that silica nanoparticles may be well tolerated, and in some case are excreted or are biodegradable. Robust synthetic techniques have allowed silica nanoparticles to be developed for applications such as biomedical imaging contrast agents, ablative therapy sensitizers, and drug delivery vehicles. This review explores the synthetic techniques used to create and modify an assortment of silica nanoformulations, as well as several of the diagnostic and therapeutic applications.

Keywords

Silica; Nanoparticles; Biomedical imaging; Biodistribution; Toxicology; Ablative technology

1. Introduction

In the past 30 years, there have been advances in the development of polymeric, liposomal, and inorganic nanoparticulate formulations for diagnostic and therapeutic applications. There are several motivations behind the development of nanoformulations for biomedical applications, such as increasing the *in vivo* lifetime of drugs and macromolecules, high payload targeted delivery of therapeutics to broaden therapeutic index, theranostic and multimodal applications beyond the scope of individual molecules, and new therapies or diagnostics. Among the many formulations under investigation, silica-based nanoparticles have promise and have garnered much attention.

Silica nanoparticles are being considered for several biomedical applications due to their biocompatibility, low toxicity, and scalable synthetic availability. It is possible to precisely

© 2014 Elsevier B.V. All rights reserved.

*Corresponding author. Tel.: +1 858 534 3368; fax: +1 858 534 2063., akummel@ucsd.edu (A.C. Kummel).

NIH-PA Author Manuscript
NIH-PA Author Manuscript
NIH-PA Author Manuscript

NIH-PA Author Manuscript

NIH-PA Author Manuscript

NIH-PA Author Manuscript

control silica particle size, porosity, crystallinity, and shape to tune the nanostructure for diverse applications. Furthermore, the many possible surface modifications of silica nanoparticles allow precise control of surface chemistry to modulate drug or chemical loading, nanoparticle dispersion, blood circulation, and site specific targeting. The ability to combine these properties makes silica nanoparticles a desirable platform for biomedical imaging, assaying, therapeutic delivery, monitoring, and ablative therapies. With the use of various dopants, surface group modifications, and assembly techniques, it is possible to create multimodal nanoparticles with theranostic applications, such as including an imaging component along with a therapeutic payload or ablative component within the particle.

This review is organized in five parts: (1) Synthesis and characterization methods for particles of uniform shapes and sizes. (2) Biodistribution and toxicology as well as the parameters which alter these properties. (3) Applications in common biomedical imaging and integration as imaging contrast agents. (4) Applications in ablative technologies. (5) Application in controlled drug delivery.

2. Synthetic techniques

Several synthesis techniques have been developed which produce particles with a narrow range of sizes and nearly uniform composition. Most of the synthetic techniques employ sol-gel processing at 25 °C with careful control of the reactant to solvent ratios or the use of templates so as to control particles sizes. Scheme 1 depicts the techniques that are commonly used to synthesize silica nanoparticles. Note: the reagents and approaches listed in this scheme are among the most common, but many others are substituted for specific applications.

2.1. Stöber method

The Stöber method, developed in 1968, continues to be a widely employed method for synthesizing silica nanoparticles [1–6]. Briefly, tetraethyl orthosilicate (TEOS) or other silicates are combined in a mixture of water, alcohol, and ammonia and agitated to form particles whose size depends on the concentration of the solvents and silicate additives. The Stöber method can be employed without templates to form solid particles. There have been many investigations of the kinetics and characterization of Stöber process generated particles in order to precisely control their size, shape, and uniformity. For example, Nozawa et al. studied the rate of addition of TEOS *vs*. the resulting size of synthesized particles [3]. The particle size decreased with an increase in the rate of addition of the TEOS, and precisely controlling the rate of addition produced uniform particles. As seen in Fig. 1a–c, by increasing the rate of TEOS addition from 0.005 ml/min (Fig. 1a) to 0.05 ml/min resulted in a 30% decrease in particle size (Fig. 1b). A further increase in the rate of addition to 0.5 ml/min resulted in a 60% decrease in particle size (Fig. 1c). The higher rate of TEOS addition probably provides a higher density of nucleation centers consistent with smaller particles.

Further experiments with Stöber type processes have demonstrated that controlling the ratio of solvent/TEOS permits fine control of particle size [6]. Generally, as the solvent to TEOS ratio increases, the diameter of the synthesized particle decreases non-linearly (with the

NIH-PA Author Manuscript

NIH-PA Author Manuscript

NIH-PA Author Manuscript

exception of methanol/TEOS ratios below 1125), as shown in Fig. 2. As the ratio of methanol/TEOS changed from 1125 to 6000, uniform and well dispersed particles were synthesized which decreased from 1500 nm to 10 nm in diameter.

It has been suggested that sol-gel based nanoparticle growth can be modeled using the equations that describe homogenous nucleation. While the kinetics are difficult to model, the critical size above which it is thermodynamically favorable for the particle to grown can be modeled analytically. Briefly, when a solution is supersaturated with a solute, the Gibbs free energy is high in solution and nucleation of particle growth can occur in response to reduce the free energy. The free energy for nucleation (ΔG) depends on the radius of the nuclei (*r*) as well as the volume free energy (ΔG_v) and the surface free energy (γ)

$$\Delta G = \frac{4}{3}\pi r^3 \Delta G_v + 4\pi^2 \gamma$$

At a given critical nucleation radius, *dG/dr* = 0, so the critical free energy barrier will be overcome and particule nuclei will begin to form to reduce the free energy to balance out the solubility of the solute. For uniform particle growth, it is best to have a short nucleation time so that, during subsequent particle growth, all the nuclei are allowed to grow for an equal amount of time. R_N is the number of nuclei grown per unit volume per unit time, C_o is the initial concentration of solute, λ is the diameter of the growth species, η is the viscosity and ΔG^* is the critical free energy which must be overcome for nucleation to begin.

$$R_N = \left[C_o kT/(3\pi\lambda^3\eta) \right] e^{(-\Delta Go*/kT)}$$

Continued growth of particles depends on the diffusion and reaction kinetics which are a function of time, concentration, temperature, solution viscosity, *etc*. [7]. In the work shown in Fig. 1, it is likely that the increased rate of addition of TEOS solution resulted in an increased initial concentration of nuclei, which resulted in a larger R_N value and thereby accounts for the decreased particle size. The work presented in Fig. 2 follows this same trend until the molar ratio of methanol/TEOS exceeds 1125. With a methanol/TEOS ratio from 300 to 1125 the particle size increases as the initial concentration decreases. This most likely can be attributed to a decreased R_N. In the study performed in Fig. 2, with a molar ratio of methanol/TEOS exceeding 1500 the particle size decreases. It is hypothesized that at very low concentrations, the λ^{-3} term (λ is the diameter of the growth species) becomes the dominant term in the equation which allows smaller nuclei to form and increases R_N. Additionally in the study in Fig. 2, water was kept at a constant ratio with TEOS and the methanol volume was kept constant. Therefore, the quantity of water to hydrolyze TEOS was also reduced, which could have also influenced the outcome. The relatively low concentrations of both TEOS and water could have resulted in a very short growth phase following nucleation, which resulted in smaller particles.

The high degree of control over growth and reaction kinetics in the Stöber process enables synthesis of the many varieties of silica particles that have since been prepared. While there are many unique synthetic techniques for creating silica nanoparticles, most techniques to

NIH-PA Author Manuscript

NIH-PA Author Manuscript

NIH-PA Author Manuscript

synthesize mesoporous, hollow, and various shaped particles are fundamentally derived from the Stöber process but include additional structure directing components.

2.2. Mesoporous particles

The advantage of using mesoporous silica nanoparticles is predominantly the very large surface area from controllable pore size and volume. This allows a large drug payload to be loaded into or adsorbed to the particles. Mesoporous silica nanoparticles can be synthesized by modifying the Stöber process with added surfactants (*e.g.*, cetyl trimethylammonium bromide [CTAB]), micelle forming type materials, polymers, and other dopants [8–10]. The micelles act as masks for the TEOS based silica growth; after micelle removal, pores are generated within the silica nanoparticles. Varying the materials and concentrations used to create the pores allows for fine control of the pore size, structure, and particle crystallinity. Pore sizes have been reported to vary between 10 and 300 A depending on the structure directing material. Post synthetic modification of the nanoparticles can also be used to adjust the pore size [11]. During mesoporous particle growth, there is an increased condensation of silicon resulting in a larger degree of Si–O–Si bonds and fewer Si–OH groups relative to typical nonporous Stöber particles [12]. The degree of Si condensation can also be affected by calcination which reduces the number of Si–OH groups.

Tightly controlling the surfactant and TEOS concentrations can yield uniform structured mesoporous particles. Cai et al. used TEOS in the presence of CTAB, which is amphiphilic and forms micellular structures, to prepare highly ordered MCM-41 type nanoparticles. MCM-41 (Mobil Composition of Matter Number 41) is one of the most highly investigated classes of silica nanoparticles. The hexagonal pore structure of MCM-41 can be observed by electron diffraction and high resolution TEM, as can be seen in Fig. 3 [8]. Typically, MCM-41 type particles have highly ordered pore structures, with pore sizes ranging from 1 to 3 nm.

For larger pore sizes, triblock polymers composed of polyethylene oxide and polypropylene oxide are employed as the network structuring components [13]. The block copolymers form templates which are combined with TEOS to form materials with pore sizes between 46 and 300 Å. This material, SBA-15 (Santa Barbara Amorphous type material-15) is also a highly investigated silica nanoparticle. The pore sizes vary with the specific polymer employed in the synthesis and are uniform for a given polymer. Typically, using surfactants as the structure-directing element results in pores are limited to below 40 Å. Larger pore sizes allow for the ability to load larger materials such as proteins or smaller particulates after coarse synthesis of the silica nanomaterial.

Jambhrunkar et al. developed a technique to precisely control pore sizes in mesoporous silica nanoparticles [11]. It was hypothesized that an ideal pore size would improve the solubility of hydrophobic drugs in solution which had been adsorbed onto the silica nanoparticles. Multiple cycles of addition of vaporized TEOS or tetramethyl orthosilicate (TMOS) were added to the particles using vacuum-assisted vapor deposition (WD) followed by calcination. Using this approach with known materials, such as MCM-41 and SBA-15, conserved the hexagonal nanostructure and the pore size could be reduced by 0.29 nm with TEOS and 0.54 nm with TMOS per cycle for at least 3 cycles of the WD process. With

NIH-PA Author Manuscript

NIH-PA Author Manuscript

NIH-PA Author Manuscript

various structure directing agents and post synthetic modifications, very precise pore sizes and surface areas can be achieved with mesoporous particles. Fine synthetic control resulting in high surface areas, well controlled particle sizes and various shapes have resulted in mesoporous silica nanoparticles being a focus of investigation [8,11,14].

2.3. Hollow or core-shell particles

There have been many approaches in creating templated or hollow silica nanoparticles using techniques such as condensation of trialkoxysilanes onto polymer based templates, metal organic frameworks (MOFs), and other nanomaterials or even island type growth using smaller nanoparticles onto a template followed by dissolution or calcination [15–19]. These techniques can produce particles which are hollow and capable of carrying very large payloads or contain cores made of desirable materials such as gold, silver, or various polymers.

Caruso et al. initially investigated a technique for layer by layer assembly of hollow silica nanoparticles on a polymer template using 25 nm colloidal silica nanoparticles to form a shell [20]. When 2 or more sequential layers of silica were deposited onto a polyelectrolyte coated polystyrene templates before calcination, particles would form uniformly. Furthermore it was observed that repeat coatings could produce a shell thickness varying from 25 to 210 nm. Caruso et al. explored this templating method using commercially available polystyrene particles and variable sized colloidal silica nanoparticles to eventually synthesize hollow silica nanoparticles [21]. The negatively charged templates were first coated with polyelectrolytes such as poly (diallyldimethylammonium chloride), poly (sodium 4-styrenesulfonate), and poly (allylamine hydrochloride) in order to better facilitate the adsorption/deposition of silica. Silica nanoparticles in three size regimes (100–70 nm, 50–40 nm and 10–20 nm) were investigated. Nanoparticles of all three sizes were added sequentially to the templates with a layer of polyelectrolyte between each silica particle deposition step. After the silica deposition was completed, the particles were calcined to remove the polystyrene template resulting in hollow silica particles. TEM showed that the smaller silica particles filled in the gaps made by the initial deposition of the larger (100–70 nm) silica particles allowing for the particles to have a larger surface area.

Yang and co-workers developed a method to rapidly synthesize hollow silica spheres by first coating commercially available polystyrene templates with poly-L-lysine and then performing a polycondensation reaction with hydrolyzed tetramethyl orthosilicate [22]. After calcination, the resulting hollow nanoshells typically had a 6–10 nm thick shell as seen in Fig. 4, but the diameter of the particles isotropically decreased 10–20% after calcination. This technique was adaptable for templates ranging between 100 and 500 nm in size. This technique, with some variation, is most commonly used for the synthesis of core–shell particles. The core is composed of polystyrene latex which is vaporized under calcination resulting in a hollow particle. However, it is possible to use other materials as the core for templating such as metals, which would result in core–shell particles which also have a broad spectrum of applications.

NIH-PA Author Manuscript

NIH-PA Author Manuscript

NIH-PA Author Manuscript

2.4. Shaped particles

Modifying the shape of nanoparticles can dramatically affect their *in vivo* properties such as biodistribution, bioavailability, and endocytosis potential [23–25]. Typically, the nanoparticles synthesis is modified by adding various dopants as precursors, dramatically changing pH or temperature during synthesis, or starting with a uniquely shaped template. Trewyn et al. investigated various room temperature ion liquid templates for silica nanoparticles synthesis and the resultant effects on silica pore size, morphology, particle size, and shape. [14]. Various crystallized organic C_n-methylimidazolium (n=14,16,18) derivatives were combined with TEOS in a sodium hydroxide solution. The surface area and pore size increased with the length of the alkyl chain. Furthermore, C_{14}MIM and C_{16}MIM derived particles yielded spherical structures but C_{18}MIM and C_{14}OCMIM derived particles produced rod- or worm-like structure. Using a different approach, Reiter et al. prepared hollow silica nanorods with different aspect ratios [26]. These nanorods could be synthesized by coating nanoscale metal organic frameworks (MOF) with TEOS and performing a low pH dissolution to remove the core metal organic framework. By controlling the water ratio in the microemulsion of the initial synthesis of the metal organic framework, a variety of different aspect ratios could be achieved varying from 2.5 to 40 with a final 8–9 nm silica shell thickness as demonstrated in Fig. 5.

2.5. Etched particles

Etching is another synthetic technique used structure nanoparticles by removing specific chemical structures or elements preexisting in the nanoparticles with chemical or physical treatments. The particles can be synthesized by the Stöber process or other techniques (*e.g.* mesoporous, hollow or otherwise shaped particles) and the structural properties are modified by the post synthetic etch [27]. Chen et al. developed a structural difference based selective etching [12]. Solid silica nanoparticles were used as a template or seed on which a sol–gel reaction was performed for mesoporous silica growth using C_{18}TMS and TEOS. Afterwards, the solid silica core was etched by a hydrothermal treatment in an ammonia solution resulting in a hollow mesoporous silica nanoparticle. The etching selectivity is based on a higher ratio of Si–OH groups than Si–O–Si in the solid silica core compared to the mesoporous silica shell; the higher ratio of Si–OH to Si–O–Si in solid silica *vs*. mesoporous silica is a result of a greater degree in condensation during mesoporous particle growth [12]. Using this same method, Chen et al. synthesized uniformly ellipsoidal mesoporous silica particles for biomedical imaging and drug delivery by first templating the growth of solid silica and mesoporous silica onto an ellipsoidal iron oxide nanocrystal core before etching to remove the solid silica [28]. This resulted in an ellipsoidal mesoporous silica nanoparticle with an iron oxide core.

Wong and co-workers synthesized yolk–shell nanoparticles as well as concentric multishell particles [29]. Yolk–shell particles are particles that are hollow but have a smaller particle within them resembling an egg yolk or a rattle. The particle synthesis begins with an Au nanoparticle (Fig. 6a), then Stöber growth is performed with TEOS resulting in a Au core–silica shell particle (Fig. 6b). The particles are treated with 2-propanol followed by hydrothermal treatment which results in a yolk–shell particle (Fig. 6c). The purpose of the 2-propanol treatment is to render the outer layer of silica unetchable, while the hydrothermal

NIH-PA Author Manuscript

NIH-PA Author Manuscript

NIH-PA Author Manuscript

treatment etches away the silica just adjacent to the Au core. It was hypothesized that the part of the etching selectivity was due to the inhomogeneity of silica condensation during Stöber synthesis resulting in a less crosslinked network toward the center of the particle. Furthermore, the degree of crosslinking on the particle surface was increased during treatment with 2-propanol at 60 °C. It was shown that with alternative hardening solution it was possible to harden the entire silica shell such that none of it could be etched during hydrothermal treatment. To synthesize the multishell particles, the particles undergo three cycles of silica coating followed by treatment with 2-proponal for hardening (Fig. 6d). After shell growth and hardening, the particles are etched in water to reveal distinct layers of silica (Fig. 6e).

Others have produced similarly structured yolk–shell particles using sodium borohydride as the etching agent or by using protecting groups to conserve a layer of silica [30,31]. Zhang et al. demonstrated that poly(vinyl pyrrolidone) (PVP) could be used as a protecting ligand against NaOH etching of silica nanoparticles [32]. The PVP was adsorbed unto the surface of the particles by reflux in aqueous solution. After PVP adsorption, soaking the particles in sodium hydroxide solution resulted in porous and hollow silica shells without affecting the diameter of the nanoparticles. After 60 min of etching in a 0.02 g/ml NaOH solution, the particles lost ~ 30% of their mass with the loss increasing to ~90% after 180 min. It was hypothesized that the PVP protected the surface due to H-bonding between the carbonyl groups on the PVP and the silanol groups. This interaction prevented/reduced local interactions OH^- ions that would etch the silica.

Besides alkaline or hydrothermal etching of silica, silica particles have been synthesized by etching under acidic conditions. Chen and coworkers developed hybrid solid silica spheres (HSSS), which could be selectively etched in hydrofluoric acid solution [33]. HSSS were synthesized in three layers starting with (1) a TEOS derived silica core followed by (2) a layer synthesized from a combination of TEOS and N-[3-(trimethoxysilyl)propyl] ethylenediamine (TSD) and lastly (3) a TEOS only shell. After soaking in HF solution, the intermediate layer which was made TEOS and TSD was etched out resulting in yolk–shell type particles 460 nm in diameter with a shell thickness of 50 nm and a solid core with a diameter of 300 nm. These dimensions were tunable through a broad range due to the use of the Stöber method. Alternatively, Yu et al. demonstrated that silica nanoparticles could be etched to generate hollow or yolk–shell type particles using more conventional acids such as HC1 or H_2SO_4 combined with hydrothermal treatment [34]. Stöber synthesized particles were dispersed in pH~3.0 solution and mixed over 24 h and subsequent hydrothermal treatment was performed at 180 °C. The degree of etching varied with hydrothermal treatment time; at 10 h, 63% of Si content had been removed from the particles resulting in hollow mesoporous particles.

Overall, etching can allow for a variety of features in an individual particle that might not be available from a single synthetic technique. For example, preparing particles that are both hollow and mesoporous or that have a yolk–shell type structure.

NIH-PA Author Manuscript

NIH-PA Author Manuscript

NIH-PA Author Manuscript

2.6. Surface modification techniques

Surface modification of silica particles is most easily achieved by reaction with one of the many commercially available alkoxysilanes/halosilanes. A wide variety of alkoxysilanes/halosilanes are available from Sigma Aldrich, Gelest, Strem Chemicals and many other chemical corporations. Alkoxysilanes will bind forming 1–3 Si–O–Si links to the surface in a condensation reaction with the surface silanol groups The halosilanes will typically hydrolyze substituting the halide for alcohol group which can similarly undergo condensation forming 1–3 Si–O–Si links with surface silanol groups [35]. In anhydrous conditions, halosilanes will react directly with surface silanol groups. Most frequently, nanoparticles are functionalized with 3-aminopropyl triethoxysilane (ATPS), 3-mercaptopropyl trimethoxysilane (MPTS), and various PEG-silanes. The first two allow for facile linker chemistry with other frequently used linking moieties such as n-hydroxysuccinide (NHS) functionalized molecules, isothiocynates, malemides, *etc*. [36]. Pegylation of nanoparticles is frequently used to improve stability in biological fluids, biocompatibility, and circulation times of nanoparticles *in vivo* [37–39].

Functionalizing the particle surface allows for specific and unique applications of silica nanoparticles that would otherwise be inaccessible. For instance, Knežević et al. surface modified silica nanoparticles with pH or light sensitive triggers to release doxorubicin by capping aminopropyl trimethoxysilane (APTS) functionalized particles with nitroveratryl carbamate, which breaks away from the amino propyl group in the presence of UV radiation or in acidic environments [40]. The UV light or low pH triggers the release of the nitroveratryl carbamate protecting group creating an electrostatic repulsion with the adsorbed doxorubicin and the nanoparticle surface thereby releasing the drug from the nanoparticle. After 80 min of UV irradiation, approximately 75% of the drug loaded into the particles had been released into phosphate buffer at a pH of 7.4.

An example of using APTS for a unique application was in the linking of 1–125 labeled Bolton–Hunter reagent onto silica nanoparticles to study the biodistribution over the course of 30 days [41]. The Bolton–Hunter reagent was mixed with $Na^{125}I$ in the presence of chloroamine to radiolabel the reagent. The radiolabeled compound was mixed with APTS modified silica nanoparticles; the NHS moiety on the Bolton–Hunter reagent dissociated and allowed the reagent to attach to the surface of the particles. For the biodistribution studies, the particles were administered intravenously to mice and the individual organs were analyzed with a gamma counter for the presence of radiation from the ^{125}I bound to the particles.

Tsai et al. used MPTS to anchor a monoclonal antibody (anti-Her2/neu) to specifically target silica particles to breast cancer cells [42]. The antibody was first linked to NHS-PEG-malemide and mixed with MPTS functionalized mesoporous silica nanoparticles. In a flow cytometry study, monoclonal antibody (mAB) functionalized particles penetrated over 80% of Her2/neu positive cells and less than 20% of Her2/neu negative cells within 1 h demonstrating potential for selective drug delivery.

Lin et al. prepared dual organosilane modified mesoporous silica nanoparticles to improve the delivery of doxorubicin while maintaining high biocompatibility and *in vitro* stability in

NIH-PA Author Manuscript

NIH-PA Author Manuscript

NIH-PA Author Manuscript

biological fluids [43]. The dual silane modification maintains good dispersion in solution using a hydrophilic organosilane (PEG) while reducing the hydrolysis of silica using a hydrophobic functionalization (trimethylchlorosilane) for greater *in vivo* survival. Hydrophilic doxorubicin–HCl and hydrophobic HCl-free doxorubicin were loaded into the nanoparticles. Despite the fact that the two drugs had approximately the same loading into the nanoparticles, the doxorubicin–HCl loaded particles displayed about a 10 × lower IC_{50} values with incubation times at 24, 48 and 72 h. This was attributed to slow release of the hydrophobic HCl-free doxorubicin from the particles due to low solubility of doxorubicin in solution as well as a higher degree of hydrophobic interactions with the trimethylchlorosilane modified particles. It is clear that the surface modification of silica can alter the drug release kinetics.

3-bromopropyltrichlorosilane was linked to the surface of silica nanoparticles as a coupling agent between silica nanoparticles and other moieties. The bromopropyl modified particles could be reacted with sodium azide resulting in azide functionalized particles, which are versatile for functionalization via click reactions. [44,45]. Using this technique, Balamurugan et al. *d*emonstrated that alkyne functionalized α-helices could be coupled to the surface of silica particles [45]. This was done to demonstrate coupling polypeptides to silica and to model the interactions of proteins at the interface of an inorganic surface.

In sum, the ease and diversity of surface properties can be employed to intelligently design particles with specific functions and properties and in many ways is the basis for the diversity of applications for silica nanoparticles.

3. Biodistribution and toxicology

It is known that the size, shape, morphology, charge, and surface properties of a nanoparticle can dramatically affect its biodistribution, toxicology, and bioavailability. By understanding these parameters, nanoparticles can be designed for improved circulation, decreased toxicity, and targeted delivery, thereby creating more efficacious and safe therapeutic and diagnostic agents.

3.1. Biodistribution

A variety of methods are available to study biodistribution of silica nanoparticles: most commonly the techniques employed are ICP–OES/MS, radiolabeling, and fluorescence. The advantage of ICP–OES/MS is that the organs are typically digested for analysis, which allows direct measurement of the atomic composition of organs. However, radiolabeling and fluorescence allow for real time imaging and dynamic analysis of the native nanoparticle biodistribution. Furthermore, with gamma counters, after sacrificing the animals, the amount of injected dose/gram organ can be quantified by measuring the remaining organ radioactivity.

Decuzzi and co-workers evaluated the effect that silica particle size and shape have on biodistribution [24]. Spherical particles of 0.7–3 urn diameters were administered at doses of 10^7 or 10^8 particles per animal to MDA-MB-231 breast tumor bearing mice. After 2–6 h, the animals were sacrificed and the organs were analyzed by ICP–OES. As can be seen from

NIH-PA Author Manuscript

NIH-PA Author Manuscript

NIH-PA Author Manuscript

Fig. 7, the particles were primarily retained by reticuloendothelial system (RES) organs such as the liver, spleen and lungs. As the dose increased a factor of 10 × from Fig. 7A to B, the accumulation of particles in all sizes increased primarily in RES organs. For both a high dose and a low dose of particles, as the particle diameter decreased, a greater number of particles were retained in each organ with the exception of the lungs.

Pegylation can greatly reduce the aggregation of silica under biological conditions *in vitro* and *in vivo*. Lin et al. demonstrated that hydrothermal treatment along with pegylation of sub-50 nm silica particles allows the particles to retain their hydrodynamic radius even after 10 days of incubation in completed cellular media, whereas non-treated particles under the same conditions aggregate rapidly [46]. Additionally, it was shown that pegylated particles have a substantially decreased uptake by macrophage cells as compared to bare particles, which provides a potential for longer circulation and evasion of the RES. He et al. also studied the distribution of pegylated *vs*. nonpegylated particles as a function of size (80–360 nm) in ICR mice. It was shown that large particles were absorbed more rapidly by RES organs, but this absorption was reduced by pegylation. Furthermore, decreasing particle size and including pegylation resulted in increased blood circulation time [39].

Consistent with the effect of pegylation, surface charge and morphology can greatly affect silica nanoparticle biodistribution. Yu et al. examined the effect of porosity and surface charge on the biodistribution of silica nanoparticles [48]. Mesoporous particles and nonporous Stöber particles of the same size (~ 120 nm) were compared with and without amine surface modification. Both particles accumulated in RES organs, and mesoporous particles had a substantially greater accumulation in the lungs compared to nonporous particles. However, surface amination reduced lung accumulation for mesoporous particles but resulted in increased liver and spleen accumulation. Souris et al. demonstrated that surface charge on silica nanoparticles could even effect the *in- vivo* retention of nanoparticles, with positively charged aminated particles undergoing rapid excretion through the hepatobiliary tract [47]. Positively charged mesoporous silica nanoparticles with a zeta potential of + 34.4 mV had an onset of clearance into the intestinal tract in less than 30 min compared to over 3 days with −17.6 mV negatively charged particles. There have been several reports which have confirmed the urinary and fecal excretion of various formulations and sizes of silica particles [39,49,50]. Huang and co-workers investigated the biodistribution of different silica nanoparticles with varying aspect ratios using ICP–OES and demonstrated that even larger silica nanoparticles could be excreted [51]. Consistent with other reports, the majority of the particles injected ended up in the RES organs, but longer nanorods (~720 nm × 140 nm) compared to shorter nanorods (~185 nm × 120 nm) showed decreased accumulation in the liver and much more accumulation in the spleen at 2 h, which leveled off over 24 h. After 7 days, the % injected dose/gram in all the organs for all formulations had decreased but could still be detected in the urine and feces (confirmed by TEM and ICP–OES). This clearly demonstrates excretion of these large nanoparticles. Overall, there are differences observed in the biodistributions of silica particles with different sizes, shapes, and surface functionalizations. Particles predominantly accumulate in the livers, lungs, and spleens of animals, and some investigators have observed diminished silicon content in the bodies of animals over time due to excretion.

NIH-PA Author Manuscript

NIH-PA Author Manuscript

NIH-PA Author Manuscript

3.2. Toxicology

Toxicology of silica nanoparticles is nuanced because the toxicology can dramatically change based on particle formulation, particle size, particle shape, and particle type. Nevertheless, there are many reports for various formulations showing that silica nanoparticles are generally well tolerated with a large maximum tolerated dose.

Lu et al. have performed multiple dose acute toxicity studies with mesoporous silica nanoparticles between 100 and 130 nm in size. Nude mice were dosed once per day for 10 days with doses as high as 200 mg/kg. Although the larger doses were not particularly harmful to the mice, the mice receiving doses over 100 mg/kg did have higher aspartate transaminase (AST) levels, which indicates liver inflammation or damage. In a longer-term toxicity study, mice were dosed twice weekly with 1 mg of particles/mouse (~ 50 mg/kg) for two months and showed no abnormal behavior, histology or hematology [52]. Lui et al. found similar results at equivalent doses in an extensive toxicological examination with 110 nm mesoporous silica nanoparticles [53]. Lower single doses of particles (below 500 mg/kg) had very little impact on serum chemistry and histological evaluation. However, higher doses (above 500 mg/kg) had a clear impact on markers such as alanine transaminase (ALT), AST, and white blood cell count. ALT and AST are both indicators of liver health, and the sudden elevation of these parameters suggested liver damage or inflammation and was confirmed by tissue histology as seen in Fig. 8. Although little damage was observed in the spleen (Fig. 8B), there was substantial degenerative necrosis and granulation found in the liver (Fig. 8A) with the 500 and 1280 mg/kg doses.

Hemolysis is the rupture of red blood cells; cytotoxicity is a measure of cellular toxicity in response to a material or chemical; both properties are invaluable in assessing the biocompatibility of a foreign substance. Since many nanoparticle formulations are most likely going to be administered intravenously, it is critical to establish hemolytic activity of administered particles, as well as their stability in whole blood. The release of heme proteins during hemolysis is associated with kidney failure in humans [54]. The hemolytic activity of mesoporous silica nanoparticles and amorphous colloidal silica particles was originally investigated by Slowing et al., who found that mesoporous particles had substantially less hemolytic activity than amorphous silica nanoparticles [55]. Hemolysis was measured by UV–vis spectroscopy after incubating rabbit red blood cells with particles and measuring the absorbance of hemoglobin at 541 nm in the supernatant. It was proposed that the increase in hemolytic activity of amorphous colloidal silica could be due to an increase in interactions between surface silanol groups and ammonium head groups of phospholipids, which promotes rupture of cell membranes. Lin and Haynes examined the hemolytic activity and cytotoxicity of several multifunctional silica nanoparticles [56]. Nonporous silica particles synthesized by the Stöber process were compared to mesoporous particles. The nonporous particles had a far greater hemolytic activity (nearly 100%), which is consistent with an increased cellular interaction from the greater number of surface silanol groups on the nonporous particles; nonporous and mesoporous particles have similar, but different synthesis processes resulting in the different ratios of Si–OH to Si–O–Si groups on the surfaces of the materials [12]. By treating the nonporous particles with a PEG-silane, the silanol groups were masked. The hemolytic activity was reduced and undetectable below a

NIH-PA Author Manuscript

NIH-PA Author Manuscript

NIH-PA Author Manuscript

concentration of 600 μg/ml. Pegylated mesoporous particles exhibited no hemolytic activity even at doses as high as 1000 μg/ml. In contrast to the results of Lin et al. Yu and coworkers investigated the *in vitro* toxicology and hemolytic activity of nonporous and various mesoporous silica nanoparticles [57]. Yu et al. compared the toxic effects *in vitro* between nonporous nanoparticles, mesoporous nanoparticles, and mesoporous rods of different aspect ratios. At concentrations below 190 μg/ml, nonporous particles had greater hemolytic activity than mesoporous particles; however, at greater concentrations mesoporous particles had greater hemolytic activity which stands in contrast to the above described work by Slowing, Lin, and Hayes. Furthermore, for mesoporous particles, increased aspect ratio decreased hemolytic activity. No acute toxicity was observed below 100 μg/ml *in vitro* for any of the particles, but cell type dependent toxicity was observed. At concentrations exceeding 250 μg/ml, both nonporous and mesoporous particles caused a decrease in cell viability in RAW 264.7 macrophage cells but had no impact on A549 lung cancer cells.

Zhang et al. compared the toxicity of fumed/pyrolytic silica nanoparticles, traditional Stöber silica nanoparticles [58]. Fumed silica is heat treated between 1200 and 1400 °C, which creates an inherently different structure to Stöber type porous silica-gel type particles. Generally, Stöber particles were far less cytotoxic than fumed particles and resulted in less hemolysis in whole mouse blood. Very little cytotoxicity or hemolysis was found with Stöber particle doses of 200 μg/ml, whereas 60% hemolysis was detected with the fumed silica at doses as low as 25 μg/ml, which exhibited escalating dose dependent toxicity. It was proposed that the increased toxicity from fumed silica was related to the presence of strained three member rings on the surface of the fumed silica particles that could generate hydroxyl radicals when the rings break.

Mitchell et al. discovered that by doping silica nanoshells with iron (III), calcined silica becomes biodegradable in human serum, which may potentially decrease the long term toxicity associated with some silica based nanoformulations. [59]. The particles are broken down by metal chelates and, *in vitro*, the particles fully degraded after 1 month in human serum kept at physiological temperature. Calcined silica particles that can biodegrade potentially allows for great bioavailability with a lower probability of dose related toxicity and long term silicosis. Iron doping these shells also increased the endocytosis of nanoshells in cancer cells that overexpress transferrin receptors, such as various ovarian and breast cancers. A competitive inhibition study using holo-transferrin demonstrated that the particles undergo transferrin mediated endocytosis in MDA-MB-231 epithelial breast cancer cells, although traditional endocytosis was also observed because of the relatively small size (100 nm) of the particles [60].

Pegylation can greatly improve the stability of silica under biological conditions *in vitro* and *in vivo*. Lin et al. demonstrated after hydrothermal treatment along with pegylation, that sub-50 nm silica particles retain their hydrodynamic radius even after 10 days of incubation in complete cellular media whereas non-treated particles under the same conditions began to rapidly aggregate [46]. Pegylated particles also exhibited decreased uptake by macrophage cells as compared to bare particles, which suggests a potential for longer circulation and evasion of the RES.

NIH-PA Author Manuscript

NIH-PA Author Manuscript

NIH-PA Author Manuscript

In general, it has been demonstrated that silica particles have relatively low toxicity both *in vitro* and *in vivo. In vitro* toxicity has generally been limited to doses below 200 μg/ml with varying degrees of hemolysis being observed. *In vivo* doses have been well tolerated for various formulations with doses exceeding 50–100 mg/kg. The low toxicity and high biocompatibility of silica nanoparticles make it a potential vehicle for applications in biomedical imaging, drug delivery, and ablative therapies. Furthermore, the biocompatibility of these particles can be improved with surface modification, such as pegylation. The development of fully biodegradable particles offer promising long-term solutions to problematic toxicity and hemolytic responses that have been observed in previous studies

4. Biomedical imaging

The backbone of modern medical therapy is improved imaging technologies which allow for earlier and more precise diagnosis, guidance, and evaluation of disease and therapies. Imaging small tumors is especially crucial for diagnosing cancer at an early or precancerous stage where surgical methods may offer a cure. Silica nanoparticles have been designed and adapted into many existing technologies to act as contrast agents. With imaging technologies, the silica nanoparticles typically act as carriers or shielding to protect the agent that gives contrast such as a fluorophore, perfluorocarbon, or superparamagnetic material.

4.1. Ultrasound imaging

Ultrasound is a commonly available, inexpensive, and low risk medical imaging technology and it is used for diagnosis, prognosis, and intra-surgical guidance. Silica nanoparticles have been developed that can enhance image contrast with existing ultrasound technologies by incorporating perfluorocarbons within the particles; however, solid and hollow silica particles have also been shown to be detectable even by non-contrast imaging modalities [61–67]. Lui et al. showed that systemically administering commercial 100 nm solid silica nanoparticles into mice could generate a detectable ultrasound response [68]. The silica particles accumulated in the liver and could be measured by ultrasound as an increase in gray scale values in the liver between 23% and 35%. The presence of these particles in the liver was confirmed by cyro-TEM, and was most visible in the Kupffer cells. Similar ultrasound behavior was observed *in vitro* by Casciaro and co-workers with agarose phantoms [69]. Ultrasound backscatter amplitude values increased as particle size increased from 160 nm to 660 nm for the pure solid silica particles for a constant number of particles.

It has been shown that by filling hollow silica nanoparticles with perfluoropentane gas, silica nanoparticles can exhibit substantial contrast under ultrasound imaging [61–63]. The use of hollow silica particles has been explored for tumor detection and imaging with ultrasound. For example, 200 μg (appox. 8 mg/kg) of 2 μm and 500 nm particles were delivered systemically into IGROV-1 tumor bearing mice and imaged with contrast pulse sequencing ultrasound. As can be seen in Fig. 9, the particles accumulate in the tumor over one hour. By using selective image filtering techniques the signal from the particles could be further accentuated as seen in Fig. 9D.

Silica nanoparticles can be used as long lived ultrasound contrast based stationary guide markers in contrast to existing soft microbubble ultrasound contrast agents, which are short

NIH-PA Author Manuscript

NIH-PA Author Manuscript

NIH-PA Author Manuscript

lived (~ 10 min). Liberman et al. have demonstrated that PFC gas filled hollow iron–silica nanoparticles can sustain a contrast signal *in vivo* in a tumor bearing mouse model for up to ten days after intratumoral injection [64]. In this study, 400 μg of 500 nm iron silica nanoshells were injected into the Py8119 tumor bearing Nu/Nu mice and imaged with color Doppler ultrasound. As can be seen in Fig. 10, the particles were well retained, and the signal persisted for 10 days with a linear signal decay. The tumor was defined by the circular shape throughout the images in Fig. 10A – F and the color Doppler signal is well retained within this volume.

The greatest advantage of silica nanoparticles compared to commercial lipid/polymeric formulations as a contrast agent in ultrasound imaging is their potential for high *in vivo* stability (slower degradation compared to lipid/polymeric formulations), which can lead to an effective long-term imaging agent. Traditional ultrasound contrast agents are composed of liposomal and polymeric formulations. They have short *in vivo* lifetimes which require multiple doses or high volumes of contrast agent for extended imaging beyond several minutes.

4.2. Magnetic resonance imaging

There are three primary methods that have been investigated to allow for MRI with silica nanoparticles: incorporation of (1) superparamagnetic iron oxide nanoparticles [70–73], (2) gadolinium [74–77], or (3) manganese oxide [78–81].

There have been many reports using silica coated superparamagnetic iron oxide nanoparticles (SPION) as a T2 MRI contrast agent. Hurley *et al*. have characterized the effects of silica coating and post synthetic treatment on the efficacy of SPIONs as a contrast agent [70]. Different silica coatings influence the transverse relaxivity (r_2) of the particles: nonporous silica coatings inherently reduce the interaction of water with the magnetic field of the SPION, which reduces the r_2 value, and therefore a mesoporous coating is preferred. With a consistent number of SPIONS encapsulated, changing the particle diameter had little to no effect on the imaging efficiency of the particles. However, hydro thermal treatment of the particles after synthesis decreased the change in the transverse relaxivity over the course of 30 days. Hydrothermally treating the particles, however, allowed for greater survival in an acidic environment that may otherwise dissolve the superparamagnetic core. This may be a key feature in imaging many cancers, which are known to possess an acidic environment.

Kim and coworkers encapsulated manganese oxide nanoparticles within mesoporous silica nanoparticles for *in vivo* cell tracking in a mouse model [80]. The results were consistent with previous findings in that the use of a mesoporous shell was more effective in achieving larger longitudinal relaxivity (r_1) than dense or nonporous silica due to the increased access of water to the core. These particles were electroporated with adipose derived mesenchymal stem cells to label them for *in vivo* cell tracking. The cells were transplanted into putamen of C15/BL6 mice and monitored by MRI. To transplant the cells into the brain of the mice, a surgical excision is made to give access to a nanoinjector which injected 10^5 labeled mesenchymal stem cells. After injection, the incision was sealed with surgical glue. As can be seen from Fig. 11A, mice which received cells incubated with particles had a clear bright spot in an MRI cross section of the brain that could be clearly imaged even 14 days after

NIH-PA Author Manuscript

NIH-PA Author Manuscript

NIH-PA Author Manuscript

transplantation. The bright spot is a result of the T1 contrast provided by the manganese oxide within the silica nanoparticles. It was hypothesized that this technique could aid in tumor detection since stem cells tend to go to sites of tumor growth, and these stem cells have been shown to be effectively labeled with manganese oxide silica nanoparticles.

A layer-by-layer assembly technique was used to develop multifunctional luminescent/fluorescent/MRI active nanoparticles [74]. A tris(bipyridine)ruthenium(II) dichloride core was coated with a silica shell and a covalently bound layer of siloxypropyl– Gd–diethylentriamine tetraacetic acid (DTTA) layer and varying ionically stacked layers of Gd–tetraazacyclododecane tetraacetic acid (DOTA) and polystyrenesulfonate. Luminescence in the particle was attributed to the tris(bipyridine)ruthenium(II) dichloride core, while the florescence in the particle was due to fluorescein covalently linked to the Gd–DOTA complex. Increasing slopes of the relaxivity values remained constant on a per Gd^{3+} basis. This is atypical of previously reported values where the relaxivities decrease per Gd^{3+} incorporated into the particles. It was hypothesized that since most of the Gd–chelate complexes were not covalently bound, there was greater interaction with water across the various layers which allowed individual Gd^{3+} ions to operate at high efficiency. However, covalently linked Gd–Si– DTTA mesoporous silica nanoparticles also had a measurable enhancement *in vivo* [76]. A 15–20% loading of Gd–DTTA resulted in a reduction in the pore size within the particles from 2.4 nm to 1.0 nm and was still sufficient to generate T2 enhancement *in vivo* in a murine model at a dose of 31 μmol/kg.

A modification was made to these particles by substituting the chelator with diethylene triamine pentaacetic acid (DTPA) which was grafted onto the particles to have a reducible disulfide bond as well as a PEG layer for increased *in vivo* lifetime and biocompatibility [77]. The cleavable disulfide bond was purposely integrated into the design of the particle so that Gd–DTPA could be released from the particles and cleared by the renal system. Clearance in the bladder was observed *in vivo* within 15 min of particle administration at a dose of 80 μmol/kg. The use of cleavable disulfide bonds resulted in overly rapid clearance of Gd–DTPA, such that the particle could not be used as an efficacious imaging agent. It was also observed that on a per Gd basis, pegylation of the particles did increase both the transverse and longitudinal relaxivity values.

4.3. Optical imaging

These imaging techniques are less frequently employed in diagnostic imaging due to the limited penetration of light in and out of tissues but are invaluable in characterizing nanoparticle interactions and uptake pathways on the cellular level. It is possible to use longer wavelengths of light and improve tissue penetration for *in vivo* imaging and photo-dynamic therapy applications. For these imaging technologies, the particles typically encapsulate a luminescent/fluorescent core [75,82,83] or are functionalized with fluorescent or 2-photon dyes [84,85].

By encapsulating $[Ru(bpy)_3]Cl_2$ within the core of the particle along with layers of chelated Gd^{3+}, Reiter et al. were able to synthesize silica nanoparticles that were both luminescent and superparamagnetic [82]. Uptake of the particles by monocyte cells could be seen clearly by confocal scanning laser microscopy, but was further confirmed by FACS analysis. Using

NIH-PA Author Manuscript

NIH-PA Author Manuscript

NIH-PA Author Manuscript

a similar core–shell technique, Ow and coworkers synthesized 20–30 nm fluorescent particles with a spectrum of fluorescent cores and silica surface shells which had a comparable fluorescent intensity as observed in quantum dots [83]. To demonstrate the efficacy of these particles as bioima-ging or labeling agents, these particles were attached to immunoglobulin E (IgE) and incubated with rat basophilic leukemia cells. As can be seen from Fig. 12A and B, the labeled particles clearly adhere to the surface of the cells which have the matching cell surface receptor FcεRI. Conversely, when free IgE was pre-incubated with the cell before addition of the particles to competitively inhibit the FcεRI receptor in Fig. 12C and D, very few particles labeled the cells.

Slowing et al. used fluorescently labeled mesoporous silica nanoparticles to demonstrate that the particles may penetrate cells, but the nanoparticles may not be retained by the cells [85]. Two different populations of HUVEC cells were incubated with silica nanoparticles labeled with one of two different fluorophores. Cells were harvested from one group and transplanted into the other group. After transplantation, some cells had endocystosed particles with both fluorophores indicating that some cells must have released the particles they had previously endocytosed and allow different cells to uptake those particles.

In order to overcome some shortcomings of fluorescently labeled silica nanoparticles, such as photobleaching and compromised surface properties, Yang et al. integrated a small amount of Eu^{3+} into the silica shells which allowed for the shells to become photoluminescent [86]. By using $Eu(NO_3)_3$ during the sol–gel growth process, the nanoparticles had an excitation at 415 nm and an emission of 620 nm, which could also be imaged by 2-photon microscopy. By incubating these Eu–SiO_2 nanoshells with HeLa cervical cancer cells, Yang et al. demonstrated that positively charged PEI coated Eu–SiO_2 nanoshells had an increased luminescence by 34% within the cytoplasm of cells and 223% on the periphery/membrane of cells compared to control cells. This indicated that the particles adhered well to the cell surface but did not efficiently penetrate the cell walls. The lack of endocytosis was attributed to a larger particle size (332 nm by DLS) and lack of targeting moiety.

There is a large versatility in the number of possible dyes, dopants, and cores used for luminescent/fluorescent imaging of silica nanoparticles which can allow for facile *in vitro* and *in vivo* studies of silica nanoparticles. Overwhelmingly, the work performed with this class of particles has been directed toward better understanding nanoparticle interactions at the cellular uptake and the pathways that silica particles go through, which impacts understanding and nanoparticle targeting design.

4.4. Scintigraphic/PET imaging

These imaging technologies rely on the decay of a radioactive species providing for very high sensitivity. Previous reports with silica nanoparticles in this field typically link a chelating agent to the particle surface in order to attach and retain the radiotracer metal ion [87–90]. An alternative approach covalently binds iodine-124 to a Bolton-Hunter reagent, which is then bound to the particle surface [91].

NIH-PA Author Manuscript

NIH-PA Author Manuscript

NIH-PA Author Manuscript

Chen et al. developed ^{64}Cu labeled mesoporous silica nanoparticles for PET imaging [87]. The particles were functionalized with MPTMS to provide a reactive thiol group to link malemide-PEG-amine. The amine was reacted with p-SCN–benzene–triazacyclononane triacetic acid (NOTA) which acted as the chelating agent for the ^{64}Cu(II) ion. The particles were also modified by adding the targeting antibody TRC105, which targets endoglin, an angiogenic tumor marker. In 4T1 murine breast tumor bearing mice, tumor accumulation and retention of targeted particles was compared to particles that were not targeted or particles that were competitively inhibited. As seen in Fig. 13, at 5 h there are clearly is a greater amount of targeted particles in the tumor compared to non-targeted or inhibited particles. Immunofluorescence staining for the TRC105 antibody on the surface of the particles demonstrated that the particles adhered to the tumor vasculature.

Liberman et al. functionalized the surface of 500 nm iron– silica and pure silica nanoshells with ^{111}In-DTPA to study nanoshell retention and accumulation in breast cancer tumors in mice [64]. The radiolabeled nanoshells were injected intravenously into tumor bearing animals, and each animal carried two Py8119 tumors on each of its rear flanks. As can be seen from the planar scintigraphic imaging over the course of 72 h in Fig. 14A – H both iron–silica and pure silica nanoshells were retained by the tumors on the flanks. Furthermore, gamma counter data revealed that an equal amount of the particles were retained in all tumors per gram tumor. It was hypothesized that the accumulation in the tumors arose from the EPR effect since no additional targeting or surface functionalization had been performed on the particles.

To aid in studying the biodistribution of 20 nm silica nanoparticles, Kumar et al. radiolabeled particles with iodine-124, a PET imaging contrast agent [91]. The ^{124}I was coupled to a Bolton–Hunter reagent that was coupled to the particle surface with APTES. While this allowed for PET imaging of the nanoparticles, it was hypothesized that this functionalization altered the biodistribution of the particles based on a comparison of fluorescently labeled particles and particles that had been both fluorescently labeled and radiolabeled. By comparison, particles with the radiolabel had substantially increased accumulation in the spleen.

The greatest advantage of using these imaging techniques with silica nanoparticles is the high degree of sensitivity of the imaging technique relative to the amount of material necessary to achieve contrast for *in vivo* applications. Little modification is necessary to achieve contrast, which could allow for tracking of nanoparticles for other applications such as ablative technologies or drug delivery without disrupting the surface chemistry or biodistribution.

5. Ablative technologies

There are many ablative technologies already in worldwide clinical use such as gamma radiation, cryo-ablation, high intensity focused ultrasound (HIFU) and many others. Silica nanoparticles have been used as carriers for sensitizing agents, amplifying agents, and guidance agents for ablative technologies. One advantage of using a nanoparticle formulation for ablative therapy is the versatility in carrying multiple payloads or having

NIH-PA Author Manuscript

NIH-PA Author Manuscript

NIH-PA Author Manuscript

multifunctional particles to allow for both imaging and ablative therapies. In many instances, silica nanoparticles designed as imaging agents can be adapted for an ablative technology, because the ablative technique is usually a more energetic form of the pre-existing imaging functionality.

5.1. Photothermal/photodynamic therapy

There have been a variety of approaches that combine photothermal therapy and nanoparticle formulations. Particles with a silica-core and gold surface shell have been utilized for near IR photothermal therapy [92–95]. Dong et al. have developed hybrid Fe_3O_4–Au silica nanoparticles for photothermal therapy and MRI imaging. By reacting Fe_3O_4 nanoparticles with an organic polymer and subsequently adding mercaptopropropyl trimethoxysilane, a silica iron oxide composite particle is formed and the surface thiol groups allow for seeding a gold shell on the surface. The gold shell enables photothermal therapy. This was shown *in vivo* with a tumor bearing mouse model where the Fe_3O_4–Au silica nanoparticles were intratumorally injected and the tissue temperature within the tumor was raised to 60 °C within a minute by laser irradiation at 808 nm and 2W/cm^2 [96]. In one study, the nanoshells were injected intratumorally into transmissible venereal tumors in SCID/j mice and the near IR laser (820 nm) was applied for 4–6 min with MRI, which resulted in a temperature increase of 37.4 °C ± 6.6 compared to a temperature increase of 9.1 ± 4.7 °C without nanoshells [93]. With the nanoshells, the temperature increase was sufficient to cause significant irreversible damage to the tumor, as evidenced by Fig. 15 which shows the damage in gross pathology and histology.

For photodynamic therapy, the particles are loaded with a chemical photosensitizer [84,97–99], and the photosensitzer generates cytotoxic species under excitation, such as free radicals. Brevet et al. covalently coupled porphyrin photo-sensitizers into mesoporous particles and demonstrated their viability as an ablative photoactivated agent *in vitro* in MDA-MB-231 breast cancer cells [97]. Neither particles alone, nor monophotonic irradiation for 1 h, were sufficient to cause a significant cytotoxic response. Combining particles and irradiation caused 45% cell death. When mannose targeting was added to the particle surface, 99% cell death was observed with the same particle concentration and irradiation time. This particle could be improved for *in vivo* studies by substituting the porphyrin for a two-photon excitable photosensitizer that allows deeper tissue penetration [98]. The particles were administered at doses of 16 mg/kg to HCT-116 tumor bearing mice. Mice were divided into three groups: mice which received saline, mice which received particles (MSN-1 man-nose), and mice which received particles and irradiation. Three irradiation treatments were performed at 760 nm for 3 min at 80 mW power for comparison with nonirradiated controls. After receiving injections/treatment, as can be seen from Fig. 16, the particles with the photodynamic treatment resulted in a 70% reduction in tumor mass compared to saline and particles without irradiation.

5.2. Radiocarrier/radiosensitizer

There are a wide number of clinical methods to perform radiotherapy; however, the point of all of these methods is to deposit ionizing radiation to cause DNA and cellular damage at a focal point, typically a tumor. The function of the nanoparticles in such a role is to sensitize

NIH-PA Author Manuscript

NIH-PA Author Manuscript

NIH-PA Author Manuscript

the cells to radiation. This could allow for shorter or more effective radiotherapy, which could reduce the side effects and cumulative damage to patients. The primary method of employing silica for this application is as a vessel for carrying high Z materials, which act as the actual sensitizing agent.

Mesoporous silica shells have been grown on top of gold nanorods to operate as a radiosensitizer/dose enhancer for X-ray radiotherapy [100,101]. Huang et al. incubated silica encapsulated gold nanorods with MGC803 gastric cancer cells and then irradiated with a 6 Gy dose using a clinical X-ray therapy instrumentation [100]. While the radiation dose remained constant across multiple concentrations of particles, an increase in particle dose from 0.625 μM to 12.5 μM resulted in an increase in cytotoxicity where cell viability decreased from 90% to 40%. It was established that there was no cytotoxic effect from the particles alone at a dose below 62.5 μM indicating that the particles act as a dose enhancing agent for X-ray radiotherapy at relatively benign concentration levels.

Instead of solely relying on high Z materials, Fan et al. synthesized yolk–shell particles with a core containing Yb, Y, and Gd, and a silica shell loaded with cisplatin as a radiotherapy dose enhancing agent [102]. The cisplatin loaded particles showed greater efficacy with radiation compared to non-cisplatin loaded particles. The sensitizing effect is attributed to the high Z component of the particles. Cisplatin alone is already utilized as both a chemotherapeutic agent as well as a radiosensitizing agent in clinics. When comparing the relative tumor volume growth *in vivo* 16 days after a single 8 Gy dose of X-ray radiation, mice which received cisplatin experienced a 2.6 fold increase in tumor volume compared to 1.8 fold increase tumor volume in cisplatin loaded yolk-shell particles.

A similar metal core and silica shell was used by Xiao and coworkers, but the silica surface was also functionalized with CuS nanoparticles for combinatorial radiotherapy and photothermal therapy [103]. Mice were implanted with $4T_1$ murine breast tumors and subjected to therapy. Mice received some combination of the following: an IV dose of particles (CSNT), near infrared treatment (MR) at 980 nm at 1.5 W/cm^2 for 8 min, or X-ray radiotherapy (RT) at 6 Gy for 5 min. As can be seen from Fig. 17a, after a single treatment, CSNT, NIR, and RT are insufficient at these doses to generate a substantial response. However, CSNT in combination with either NIR or RT results in a substantial decrease in increase of the relative tumor volume. However, CSNT with both NIR and RT treatment resulted in complete tumor regression and continued mouse survival as seen in Fig. 17b.

The ubiquity of radiotherapy combined with its problematic side effects creates a demand for more efficient and less toxic therapies. Furthermore, with radiotherapy, there are acceptable limits to dosing due to off target damage from ionizing radiation which limits the number and frequency of doses. Silica shells have been demonstrated to be effective carriers for high Z materials and drugs which would otherwise illicit a toxic response. When these particles are combined with radiotherapy, it may be possible to give smaller and more efficacious doses.

NIH-PA Author Manuscript

NIH-PA Author Manuscript

NIH-PA Author Manuscript

5.3. High intensity focused ultrasound

Traditional high intensity focused ultrasound (HIFU) uses a conical transducer to focus the ultrasound beam onto a focal volume where the ultrasonic energy is deposited as thermal energy. Ideally, thermal deposition only occurs at the focal volume of the HIFU, but due to the non-linear scattering properties of tissue, there are typically areas of ablation beyond the focal volume and down the beam path. Moreover, traditional HIFU therapy requires long insonation times and temperature monitoring by MRI. Silica nanoparticles have been explored as a means to overcome the limitations of current HIFU procedures.

There have been several examples in which silica nanoparticles have been used as HIFU sensitizers by encapsulating perfluorohexane (PFH) within mesoporous silica nanoparticles. In this application, the particles are echogenic and increase ultrasound scattering, which intensifies local thermal deposition [67,104,105]. Conventional HIFU therapy currently uses MRI for monitoring and guiding the HIFU thermal deposition. To improve both the guidance and the thermal deposition, Chen and co-workers developed manganese oxide functionalized PFH filled silica nanoparticles that could act simultaneously as a Tl MRI contrast agent and a HIFU sensitizer [104]. Particle accumulation in the tumor was measured by MRI after particles were administered intravenously. In Fig. 18A, as time after administration increased, signal intensity within the tumor increased confirming the presence of particles. After confirming particle presence by MRI, HIFU was applied at 150 W for 5 s, as can be seen from Fig. 18B, the PFH loaded particles had the maximal effect for tissue damage. Wang et al. used PFH loaded Au–silica nanoshells to decrease the exposure time of HIFU necessary to achieve a thermal lesion [105]. In this study, 12 mg of 250 nm Au–silica particles were administered to VX2 tumor bearing rabbits and allowed to circulate. After 30 min, HIFU was applied twice at 400 W for 2 s per application. Fig. 19A contains a B-mode image of the rabbit liver and the tumor can be readily observed within the liver in the area between the red arrows. After HIFU was applied, there were echogenic changes, as can be seen in Fig. 19B and C, where the gray scale value of the HIFU region increased dramatically.

Thermal damage is not always readily observable by ultrasound which creates the need for concurrent MRI to monitor HIFU therapy. An alternative approach to HIFU therapy is in the use of high power and low duty cycle HIFU such that mechanical damage is done to the tissue with minimal thermal deposition. Perfluoropentane filled iron-silica nanoshells have been shown to be useful for mechanical ablation, which can reduce both the time and the power of the applied of ultrasound [106]. In this study 800 μg (~40 mg/kg) of nanoshells were administered intravenously into Py8119 tumor bearing mice; after 24 h HIFU was applied for 1 min at 3.5 MPa and 1.1 MHz. As can be seen by comparing Fig. 20A and C, a blackened region is generated at the focal zone of the HIFU which under gross examination was found to be a cavity filled with liquefied tissue. Fig. 20B shows the HIFU in progress where cavitating bubble can be observed at the focal zone of the HIFU. By using strictly mechanical HIFU and creating no thermal damage, it may be possible to monitor HIFU therapies strictly with ultrasound and obviate the need for MRI thermometry.

As has been discussed, silica nanoparticles can greatly aid in the application of HIFU by increasing the amount of damage that is done with a given power of HIFU. This may allow

NIH-PA Author Manuscript

NIH-PA Author Manuscript

NIH-PA Author Manuscript

for shorter HIFU therapy or the use of lower power settings, which can reduce the off target tissue damage that occurs with traditional HIFU therapy. This increases the potential of HIFU as a viable non-invasive therapeutic approach in many cancer therapies.

5.4. Magnetic hyperthermia

Unlike other ablative approaches, hyperthermia with MRI requires the use of a contrast agent to deposit heat. Contrast agents in MRI are typically either paramagnetic or superparamagnetic, which in the presence of an alternating magnetic field (AMF), generate heat due to hysteresis losses during magnetization. Silica particles integrating or encapsulating superparamagnetic iron oxide particles have been used in this application [107–109], as well as manganese perovskite [110–112].

Silica encapsulated SPIONs are being investigated for hyperthermia treatment due to the availability of commercial SPIONs, as well as the FDA approval of various SPION formulations. The use of SPIONs in hyperthermia does have a slight drawback in that the Curie temperature is not readily adjustable. This results in potential off target heterogeneous tissue heating. To overcome this shortcoming, silica coated manganese oxide perovskite particles have been investigated. They have a tunable Curie temperature that restricts the maximum temperature of the particles in an AMF so that off target tissue is not harmed [110–112]. Villanueva and coworkers examined the effect that silica manganese perovskite particles (Curie temperature limited to 44 °C) had on a cellular level [110]. HeLa cervical cancer cells were incubated with the particles for 3 h, washed thoroughly and an AMF was applied at 100 kHz and 15 mT for 30 min. After 24 h, substantial changes could be observed in the cell nuclei. Fig. 21A and B are controls and show no morphological changes whereas Fig. 21C–G, show considerable nuclear damage, apoptosis, and release of the adherent cells into solution. This demonstrates that cells which internalized the particles could be sufficiently damaged without creating a large thermal gradient as typically occurs when performing hyperthermia based therapies. The technique may need to be modified *in vivo* due to a limited maximum temperature and the large degree of thermal control within a body due to blood flow.

Le Renard et al. synthesized 900 nm superparamagnetic silica nanoparticles encapsulating SPIONs and performed hyperthermia therapy *in vivo* on colorectal cancer bearing Swiss nude mice [108]. A bolus of 84 mg of microparticles was injected intratumorally and an AMF at 141 kHz was applied for 20 min with field strengths between 9 and 12 mT. As the field strength increased, the amount of viable tumor tissue decreased and areas of damaged tissue due to hyperthermia increased. Furthermore, using these particles, mice receiving a single 20 min treatment at 12 mT had a median survival of 37 days compared to 12 days without treatment. Furthermore, 45% of the animals had a 1 year survival after treatment. Wu and co-workers also found positive results in performing hyperthermia treatments with intratumorally delivered magnetic silica nanoparticles [113]. Silica particles were synthesized on top of a Fe–CaS core resulting in 48 nm Fe–CaS core, SiO_2 shell particles. Between 300 and 500 μl at 150 mg/ml of particles were injected directly into CT-26 colon cancer xenografts in Balb/c mice and hyperthermia treatment was performed for 20 min with an AMF at 750 kHz with a field strength of 10 Oe. Tumor volume in control mice increased

NIH-PA Author Manuscript

NIH-PA Author Manuscript

NIH-PA Author Manuscript

by a factor of 3.5 over the course of 15 days compared to almost complete tumor reduction in mice that received particles. In Fig. 22a1 and a2 after hyperthermia treatment the tumor was replaced with a black scarred region approximately the same size as the original tumor 15 days after treatment resulting from local hyperthermia while control tumors greatly increased in volume in Fig. 22b1 and b2.

An alternative strategy was employed by Ruan et al. who, instead of performing an intratumoral injection to deliver particles directly to the tumor, first incubated aminated SPION loaded silica particles with mesenchymal stem cells, which are known to traverse to sites of wound healing and cancers [114]. Mesenchymal stem cells loaded with silica–SPION particles were injected intravenously into subcutaneous gastric cancer bearing mice. These mice received weekly AMF treatments at 63 kHz and 7 kA/m for 4 min. Mice which received both particles and AMF treatment exhibited a delayed tumor progression over the course of a month. Mice that received either particles or AMF alone had a 2–3 fold increase in tumor volume during this period.

The advantages of this hyperthermia therapy is that the particles are inherently an imaging agent for MRI which allows precise understanding of what tissues are being treated. Furthermore, there have been examples of decreased magnetization of particles with various degrees of coating of silica, which can help control the Curie temperature and reduce off target burning [110]. And with a silica coating, simple synthetic modification, such as amination, can facilitate cell uptake for alternative delivery strategies such as mesenchymal stem cell delivery [114].

6. Stimuli responsive drug delivery

Silica nanoparticles are attractive drug delivery vehicles due to their large and stable surface area, stability *in vivo* and ease of surface modification. Surface modification of silica can increase *in vivo* circulation times, lower toxicity, and increased drug adsorption/loading. There have been a variety of approaches with rigid silica particles, which do not rapidly degrade, in order to encapsulate drugs for triggered or controlled release. Frequently doxorubicin or various fluorophores are used as model drugs for loading silica nanoparticles because the drug fluorescence makes it simpler to detect and quantify.

6.1. Internally triggered drug release

Other researchers have explored various gating techniques, such as functionally plugging the pores in the nanoparticles until tissue or cell specific chemical or enzymatic triggers unplug the pores [115–117]. To create nanoparticles with very high drug retention and triggered release, Giri et al. synthesized propyldisulfanyl propionic acid functionalized mesoporous silica nanoparticles, which were capped with aminopropyl triethoxysilyl-SPIONs that acted as chemically cleavable pore caps [115]. The SPION caps were approximately 10 nm in diameter and were linked to the mesoporous silica nanoparticle surface to physically block off drug release. The caps are released by reduction of the disulfide bond in the functionalized particles by intracellular reducing agents. Capped particles showed over a 3 × decrease in surface area by N_2 adsorption/desorption to 296 m^2 g^{-1}, which was expected of nonporous material. When loading fluorescein into the particles, it was observed that there

NIH-PA Author Manuscript

NIH-PA Author Manuscript

NIH-PA Author Manuscript

was no release over the course of 132 h without the presence of a reductant *in vitro*, which demonstrates the potential for a highly controlled and specific drug delivery system. Rotaxane gated nanoparticles have been synthesized that could be triggered by esterase enzymes [117,118]. The rotaxane acts as a valve which blocks the pores containing the drugs until the particle encounters an esterase found in cellular cytoplasm. Despite the relatively large size of the particles being used (~200 nm), Porta et al. demonstrated that rotaxane capped particles were capable of penetrating the nuclear membranes of U20 cells, which was attributed to the folic acid functionalization of the particles [117]. It was shown using a TUNEL assay that they caused no damage to the DNA once inside the nuclei unless the particles had been loaded with cytotoxic drugs.

Zhao et al. synthesized mesoporous particles that were capped with gluconic acid modified insulin which dissociated in the presence of various saccharides to release insulin or cyclic adenosine monophosphate (cAMP), which triggers a pathway in pancreatic cells to produce insulin [119]. To achieve this specific release, the particles were functionalized with a phenylboronic acid which form bonds with the vicinal diols on the gluconic insulin cap. However, this bond was shown to be broken in the presence of the adjacent diols present in various saccharides. Fig. 23 demonstrates the release of FITC modified gluconic acid modified insulin as a function of concentration of various saccharides at pH 7.4. It was also demonstrated that cAMP loaded into the particles could be released as a function of glucose concentration at pH 7.4 based on the release of the gluconic acid modified insulin caps.

One method to internally trigger the release of the drug from nanoparticles is pH. Acidic environment triggered release may be advantageous for highly cytotoxic drugs because many tumors and endosomes have been reported to have acidic environments compared to blood which has pH 7.4. Fang and coworkers synthesized Pd/Ag core mesoporous particles that had been modified with APTES, dihydroxybenzaldehyde, and Fe^{3+} for pH and photo-dependent drug release of doxorubicin [120]. The APTES, dihydroxybenzaldehyde, and Fe^{3+} were bound to the particle in order to coordinate the doxorubicin with amine groups and Fe^{3+}, but in an acidic environment, these coordination bonds are less stable prompting the release of doxorubicin from the nanoparticles. Over the course of 1 h, in neutral pH, the particles released 5% of the loaded drug, but in pH 4 about 30% of the doxorubicin was released. Applying laser irradiation to the particles at 808 nm created a photo-thermal effect with the Pd/Ag core which approximately doubled the drug release in 1 h due to weaker coordination bonds at higher temperatures.

6.2. Externally triggered drug release

Another technique for controlling drug delivery from silica nanoparticles is by limiting drug release to an external trigger, such as light excitation or AMF. There have been investigations of SPION core-silica shell nanoparticles which release drug based AMF using a heat gradient to promote drug diffusion out of the nanoparticle [121,122]. Kong et al. loaded silica–SPION nanoparticles with camptothecin and doxorubicin and then demonstrated that an AMF could induce drug release by heating within the particle. As can be seen in Fig. 24a and b, during the cycles that AMF is enabled, drug is released from the particle and during the period that the AMF is off, there is no drug release. It was also

NIH-PA Author Manuscript

NIH-PA Author Manuscript

NIH-PA Author Manuscript

shown with these particles that a magnetic field can be used to increase particle accumulation in a tumor model [121] or even to penetrate the blood–brain barrier [122].

There have been several reports of phototriggered drug delivery from silica nanoparticles [40,123]. Aznar et al. capped mesoporous silica particles with gold nanoparticles which could undergo reversible cleavage by light to release drugs; a hydrophilic dye safranine O was used as a model drug [123]. The mesoporous silica particles were functionalized with a polyalcohol which would react with gold nanoparticles functionalized with boronic acid which can react with the alcohol to form boronate esters. Plasmonic heating of the gold nanoparticles was used to cleave the boronic ester linkages and release the dye entrapped in the particle. As can be seen in Fig. 24c, it was possible to achieve pulsatile release of the cargo, each of the dotted lines represents activation of the laser at 1064 nm for 5 pulses at 4.3 ns/pulse. After each irradiation there was observed release of the dye, however, after several minutes the drug release ceased until the next irradiation of the particles.

Kim et al. were able to externally trigger drug release using mesoporous silica nanoparticles cast in a polydimethylsiloxane (PDMS) film with ultrasound [124]. Mesoporous silica nanoparticles loaded with ibuprofen alone demonstrated “burst” release of the drug with an immediate release of nearly 50% of the encapsulated drug, once in cast into the PDMS, the rate of release without stimulation became nearly identical to that of PDMS: immediately releasing about 10% of the drug payload but otherwise remaining at steady state. Once the ultrasound is applied to the particles cast in PDMS, the release of the drug is almost immediate and sustained throughout the application of the ultrasound. Pulsed release of the drug was achieved by exposing the PDMS/particles to small increments of ultrasound rather than continuous exposure.

There are several techniques that have been explored for externally triggered drug release with silica nanoparticles which can allow for drug release in very specific areas with little non-specific release. The implication of these technologies is that they can potentially increase the therapeutic index of highly cytotoxic drugs by only allowing their release in a region of interest and spare off target tissues.

7. Concluding remarks

Over the past several years, research into silica nanoparticles has expanded applications and clinical relevance, which reflects a maturation of the field as a whole. The increased interest in silica nanoparticles has resulted in an increased pursuit and understanding of silica biocompatibility, biodistribution, and toxicology. It has been reported that calcined silica may be synthesized to be biodegradable or can be excreted through various pathways. Generally, it is found that silica nanoparticles are well tolerated, but the degree of tolerance varies with formulation, size, and surface properties. Because these reports are divergent, specific toxicology studies will be required for any particle in clinical applications. However, in general silica particles have extremely low toxicity compared to other nanoformulations.

NIH-PA Author Manuscript

NIH-PA Author Manuscript

NIH-PA Author Manuscript

Silica nanoparticles usually serve as a vehicle to carry or deliver an imaging or therapeutic agent and shield it from the body. Silica nanoparticles have been employed in animal studies for imaging contrast agents and sensitizing agents for ablative therapies. Silica particles have been successfully shown to be adaptable for a variety of imaging technologies, which is promising for establishing an initial clinical presence. In the development of imaging agents, the acceptable risk is much lower than for therapeutic therapies because the technology is meant to either aid in diagnosis or prognosis. However, the reports that silica particles have been very well tolerated *in vivo* and the relatively low amounts of particles that are necessary to achieve significantly improved image contrast offers promise for the commercial development of silica based imaging contrast agents.

Interest in using silica nanoparticles as therapeutic agents also remains high. The *in vivo* tolerance of silica particles makes them very attractive ablative sensitizers where they decrease the time or power of the ablative technique, but remain relatively innocuous until the external source of ablative energy is applied. Additionally, in the field of drug delivery, there have been strides in developing smarter drug delivery vehicles which are stimuli responsive as contrasted with simple “soak and release” drug delivery vehicles. Silica particles used for ablative therapy are very similar to the silica particles used for drug delivery which require an external trigger for drug release. Both approaches may increase the therapeutic index and safety of these therapies that otherwise have been known to have substantial side effects. However, both approaches require that the location of the tumor or diseased tissue be known and accessible to the external energy source. In this sense, silica particles designed with a chemical or enzymatic trigger for drug release may be more advantageous. In instances such as metastatic disease or a whole body disease, where drug needs to be delivered in multiple locations, a vehicle that releases drug in a tissue specific manner is desirable. The risk with this approach is that there may still be chemicals or enzymes that are present in off-target tissues that can release the drugs from the particles. Nevertheless, all of these approaches are intelligently designed to improve on existing therapies and they may take advantage of silica as a platform.

Overall, the various synthetic techniques and structures that can be achieved with silica nanoparticles have helped to facilitate the innovation and investigation into many biomedical applications. As the interest in this field has increased, study of the particle safety and toxicology has increased so that silica nanoparticles may find biomedical applications to improve existing imaging and therapeutic technologies.

Acknowledgments

The authors would like to acknowledge that their work in this field has been supported by National Institutes of Health Grant R21-CA151140 and by the Samsung Advanced Institute of Technology Grant 20125011. Alexander Liberman has been supported by 1F31CA174276–01A1 awarded by the National Institutes of Health; Natalie Mendez has been supported by 3R25 CA153915-03S1 awarded by the National Institutes of Health and the NSF AGEP fellowship no. 0450366 from the National Science Foundation. Alexander Liberman and Natalie Mendez both received support and training from R25 CA153915 training grant. Prof. William C. Trogler has been supported by Award no. P42ES010337 from the National Institute of Environmental Health Sciences.

References

1. Stöber W, Fink A, Bohn E. J. Colloid Interface Sci. 1968; 26:62–69.

NIH-PA Author Manuscript NIH-PA Author Manuscript NIH-PA Author Manuscript

2. Choi H, Chen IW. J. Colloid Interface Sci. 2003; 258:435–437. [PubMed: 12618117]
3. Nozawa K, Gailhanou H, Raison L, Panizza P, Ushiki H, Sellier E, Delville JP, Delville MH. Langmuir. 2004; 21:1516–1523. [PubMed: 15697302]
4. Wang X-D, Shen Z-X, Sang T, Cheng X-B, Li M-F, Chen L-Y, Wang Z-S. J. Colloid Interface Sci. 2010; 341:23–29. [PubMed: 19819463]
5. van Blaaderen A, Vrij A. J. Colloid Interface Sci. 1993; 156:1–18.
6. Shimura N, Ogawa M. J. Mater. Sci. 2007; 42:5299–5306.
7. Cao, G. Nanostructures and Nanomaterials. London, UK: Imperial College Press; 2004.
8. Cai Q, Lin W-Y, Xiao F-S, Pang W-Q, Chen X-H, Zou B-S. Microporous Mesoporous Mater. 1999; 32:1–15.
9. Radu DR, Lai C-Y, Huang J, Shu X, Lin VSY. Chem. Commun. 2005:1264–1266.
10. Yokoi T, Yoshitake H, Tatsumi T. J. Mater. Chem. 2004; 14:951–957.
11. Jambhrunkar S, Yu M, Yang J, Zhang J, Shrotri A, Endo-Munoz L, Moreau J, Lu G, Yu C. J. Am. Chem. Soc. 2013; 135:8444–8447. [PubMed: 23668366]
12. Chen Y, Chen H, Guo L, He Q, Chen F, Zhou J, Feng J, Shi J. ACS Nano. 2009; 4:529–539. [PubMed: 20041633]
13. Zhao D, Feng J, Huo Q, Melosh N, Fredrickson GH, Chmelka BF, Stucky GD. Science. 1998; 279:548–552. [PubMed: 9438845]
14. Trewyn BG, Whitman CM, Lin VSY. Nano Lett. 2004; 4:2139–2143.
15. Yang J, Lee J, Kang J, Lee K, Suh J-S, Yoon H-G, Huh Y-M, Haam S. Langmuir. 2008; 24:3417–3421. [PubMed: 18324841]
16. Zhang T, Ge J, Hu Y, Zhang Q, Aloni S, Yin Y. Angew. Chem. 2008; 120:5890–5895.
17. Tissot I, Reymond JP, Lefebvre F, Bourgeat-Lami E. Chem. Mater. 2002; 14:1325–1331.
18. Sandberg LIC, Gao T, Jelle B, Gustavsen A. Adv. Mater. Sci. Eng. 2013; 2013:6.
19. Graf C, Vossen DLJ, Imhof A, van Blaaderen A. Langmuir. 2003; 19:6693–6700.
20. Caruso F, Caruso RA, Mohwald H. Science. 1998; 282:1111–1114. [PubMed: 9804547]
21. Caruso RA, Susha A, Caruso F. Chem. Mater. 2001; 13:400–409.
22. Yang J, Lind JU, Trogler WC. Chem. Mater. 2008; 20:2875–2877.
23. Huang X, Teng X, Chen D, Tang F, He J. Biomaterials. 2010; 31:438–448. [PubMed: 19800115]
24. Decuzzi P, Godin B, Tanaka T, Lee S-Y, Chiappini C, Liu X, Ferrari M. J. Control. Release. 2010; 141:320–327. [PubMed: 19874859]
25. Kumar R, Ding H, Hu R, Yong K-T, Roy I, Bergey EJ, Prasad PN. Chem. Mater. 2010; 22:2261–2267.
26. Rieter WJ, Taylor KM, Lin W. J. Am. Chem. Soc. 2007; 129:9852–9853. [PubMed: 17645339]
27. Meng Q, Xiang S, Zhang K, Wang M, Bu X, Xue P, Liu L, Sun H, Yang B. J. Colloid Interface Sci. 2012; 384:22–28. [PubMed: 22818793]
28. Chen Y, Chen H, Zeng D, Tian Y, Chen F, Feng J, Shi J. ACS Nano. 2010; 4:6001–6013. [PubMed: 20815402]
29. Wong YJ, Zhu L, Teo WS, Tan YW, Yang Y, Wang C, Chen H. J. Am. Chem. Soc. 2011; 133:11422–11425. [PubMed: 21732677]
30. Zhang Q, Ge J, Goebl J, Hu Y, Lu Z, Yin Y. Nano Res. 2009; 2:583–591.
31. Zhang T, Ge J, Hu Y, Zhang Q, Aloni S, Yin Y. Angew. Chem. Int. Ed. Engl. 2008; 47:5806–5811. [PubMed: 18574831]
32. Zhang Q, Zhang T, Ge J, Yin Y. Nano Lett. 2008; 8:2867–2871. [PubMed: 18698725]
33. Chen D, Li L, Tang F, Qi S. Adv. Mater. 2009; 21:3804–3807.
34. Yu Q, Wang P, Hu S, Hui J, Zhuang J, Wang X. Langmuir. 2011; 27:7185–7191. [PubMed: 21553827]
35. Banga R, Yarwood J, Morgan AM, Evans B, Kells J. Langmuir. 1995; 11:4393–4399.
36. Hermanson, GT. Bioconjugate Techniques. San Diego, CA: Academic Press; 1996.
37. Cauda V, Argyo C, Bein T. J. Mater. Chem. 2010; 20:8693–8699.
38. Yagüe C, Moros M, Grazú V, Arruebo M, Santamaría J. Chem. Eng. J. 2008; 137:45–53.

NIH-PA Author Manuscript NIH-PA Author Manuscript NIH-PA Author Manuscript

39. He Q, Zhang Z, Gao F, Li Y, Shi J. Small. 2011; 7:271–280. [PubMed: 21213393]
40. Knežević NŽ, Trewyn BG, Lin VSY. Chem. Eur. J. 2011; 17:3338–3342. [PubMed: 21337435]
41. Xie G, Sun J, Zhong G, Shi L, Zhang D. Arch. Toxicol. 2010; 84:183–190. [PubMed: 19936708]
42. Tsai C-P, Chen C-Y, Hung Y, Chang F-H, Mou C-Y. J. Mater. Chem. 2009; 19:5737–5743.
43. Lin Y-S, Abadeer N, Hurley KR, Haynes CL. J. Am. Chem. Soc. 2011; 133:20444–20457. [PubMed: 22050408]
44. Ranjan R, Brittain WJ. Macromolecules. 2007; 40:6217–6223.
45. Balamuragan SS, Soto-Cantu E, Cueto R, Russo PS. Macromolecules. 2009; 43:62–70.
46. Lin Y-S, Abadeer N, Haynes CL. Chem. Commun. 2011; 47:532–534.
47. Souris JS, Lee C-H, Cheng S-H, Chen C-T, Yang C-S, Ho J-aA, Mou C-Y, Lo L-W. Biomaterials. 2010; 31:5564–5574. [PubMed: 20417962]
48. Yu T, Hubbard D, Ray A, Ghandehari H. J. Control. Release. 2012; 163:46–54. [PubMed: 22684119]
49. He X, Nie H, Wang K, Tan W, Wu X, Zhang P. Anal. Chem. 2008; 80:9597–9603. [PubMed: 19007246]
50. Xie G, Sun J, Zhong G. J. Nanopart. Res. 2012; 14:1–9. [PubMed: 22448125]
51. Huang X, Li L, Liu T, Hao N, Liu H, Chen D, Tang F. ACS Nano. 2011; 5:5390–5399. [PubMed: 21634407]
52. Lu J, Liong M, Li Z, Zink JI, Tamanoi F. Small. 2010; 6:1794–1805. [PubMed: 20623530]
53. Liu T, Li L, Teng X, Huang X, Liu H, Chen D, Ren J, He J, Tang F. Biomaterials. 2011; 32:1657–1668. [PubMed: 21093905]
54. Qian Q, Nath KA, Wu Y, Daoud TM, Sethi S. Am. J. Kidney Dis. 2010; 56:780–784. [PubMed: 20605299]
55. Slowing II, Wu C-W, Vivero-Escoto JL, Lin VSY. Small. 2009; 5:57–62. [PubMed: 19051185]
56. Lin Y-S, Haynes CL. Chem. Mater. 2009; 21:3979–3986.
57. Yu T, Malugin A, Ghandehari H. ACS Nano. 2011; 5:5717–5728. [PubMed: 21630682]
58. Zhang H, et al. J. Am. Chem. Soc. 2012; 134:15790–15804. [PubMed: 22924492]
59. Pohaku Mitchell KK, Liberman A, Kummel AC, Trogler WC. J. Am. Chem. Soc. 2012; 134:13997–14003. [PubMed: 22871140]
60. Mitchell, KKP.; Trogler, WC. UCSD Thesis Defense. 2011.
61. Liberman A, Martinez HP, Ta CN, Barback CV, Mattrey RF, Kono Y, Blair SL, Trogler WC, Kummel AC, Wu Z. Biomaterials. 2012; 33:5124–5129. [PubMed: 22498299]
62. Martinez HP, Kono Y, Blair SL, Sandoval S, Wang-Rodriguez J, Mattrey RF, Kummel AC, Trogler WC. Med. Chem. Commun. 2010; 1:266–270.
63. Ta CN, Liberman A, Paul Martinez H, Barback CV, Mattrey RF, Blair SL, Trogler WC, Kummel AC, Wu Z. J. Vac. Sci. Technol. B. 2012; 30 (02C104-02C104-6).
64. Liberman A, Wu Z, Barback CV, Viveros R, Blair SL, Ellies LG, Vera DR, Mattrey RF, Kummel AC, Trogler WC. ACS Nano. 2013; 7:6367–6377. [PubMed: 23802554]
65. Hu H, Zhou H, Du J, Wang Z, An L, Yang H, Li F, Wu H, Yang S. J. Mater. Chem. 2011; 21:6576–6583.
66. Lin P-L, Eckersley RJ, Hall EAH. Adv. Mater. 2009; 21:3949–3952.
67. Wang X, Chen H, Chen Y, Ma M, Zhang K, Li F, Zheng Y, Zeng D, Wang Q, Shi J. Adv. Mater. 2012; 24:785–791. [PubMed: 22223403]
68. Liu J, Levine AL, Mattoon JS, Yamaguchi M, Lee RJ, Pan X, Rosol TJ. Phys. Med. Biol. 2006; 51:2179. [PubMed: 16625034]
69. Casciaro S, Conversano F, Ragusa A, Malvindi M, Franchini R, Greco A, Pellegrino T, Gigli G. Invest. Radiol. 2010; 45:715. [PubMed: 20562708]
70. Hurley KR, Lin Y-S, Zhang J, Egger SM, Haynes CL. Chem. Mater. 2013; 25:1968–1978. [PubMed: 23814377]
71. Lu Y, Yin Y, Mayers BT, Xia Y. Nano Lett. 2002; 2:183–186.
72. Zhang C, et al. Langmuir. 2006; 23:1427–1434. [PubMed: 17241069]

NIH-PA Author Manuscript NIH-PA Author Manuscript NIH-PA Author Manuscript

73. Insin N, Tracy JB, Lee H, Zimmer JP, Westervelt RM, Bawendi MG. ACS Nano. 2008; 2:197–202. [PubMed: 19206619]
74. Kim JS, Rieter WJ, Taylor KML, An H, Lin W, Lin W. J. Am. Chem. Soc. 2007; 129:8962–8963. [PubMed: 17602632]
75. Santra S, Bagwe RP, Dutta D, Stanley JT, Walter GA, Tan W, Moudgil BM, Mericle RA. Adv. Mater. 2005; 17:2165–2169.
76. Taylor KML, Kim JS, Rieter WJ, An H, Lin W, Lin W. J. Am. Chem. Soc. 2008; 130:2154–2155. [PubMed: 18217764]
77. Vivero-Escoto JL, Taylor-Pashow KML, Huxford RC, Delia Rocca J, Okoruwa C, An H, Lin W, Lin W. Small. 2011; 7:3519–3528. [PubMed: 22069305]
78. Yang H, Zhuang Y, Hu H, Du X, Zhang C, Shi X, Wu H, Yang S. Adv. Funct. Mater. 2010; 20:1733–1741.
79. Taylor KML, Rieter WJ, Lin W. J. Am. Chem. Soc. 2008; 130:14358–14359. [PubMed: 18844356]
80. Kim T, et al. J. Am. Chem. Soc. 2011; 133:2955–2961. [PubMed: 21314118]
81. Niu D, Luo X, Li Y, Liu X, Wang X, Shi J. ACS Appl. Mater. Interfaces. 2013
82. Rieter WJ, Kim JS, Taylor KML, An H, Lin W, Tarrant T, Lin W. Angew. Chem. Int. Ed. 2007; 46:3680–3682.
83. Ow H, Larson DR, Srivastava M, Baird BA, Webb WW, Wiesner U. Nano Lett. 2005; 5:113–117. [PubMed: 15792423]
84. Lebret V, Raehm L, Durand J-O, Smaihi M, Gérardin C, Nerambourg N, Werts MHV, Blanchard-Desce M. Chem. Mater. 2008; 20:2174–2183.
85. Slowing II, Vivero-Escoto JL, Zhao Y, Kandel K, Peeraphatdit C, Trewyn BG, Lin VSY. Small. 2011; 7:1526–1532. [PubMed: 21520497]
86. Yang J, Sandoval S, Alfaro JG, Aschemeyer S, Liberman A, Martin DT, Makale M, Kummel AC, Trogler WC. J. Biomed. Opt. 2011; 16:066012. [PubMed: 21721813]
87. Chen F, Hong H, Zhang Y, Valdovinos HF, Shi S, Kwon GS, Theuer CP, Barnhart TE, Cai W. ACS Nano. 2013
88. Kang KW. Open Nucl. Med. J. 2010; 2:153–156.
89. Huang X, et al. Biomaterials. 2013; 34:1772–1780. [PubMed: 23228423]
90. Kong L, Mume E, Triani G, Smith SV. Langmuir. 2013; 29:5609–5616. [PubMed: 23581487]
91. Kumar R, Roy I, Ohulchanskky TY, Vathy LA, Bergey EJ, Sajjad M, Prasad PN. ACS Nano. 2010; 4:699–708. [PubMed: 20088598]
92. Loo C, Lowery A, Halas N, West J, Drezek R. Nano Lett. 2005; 5:709–711. [PubMed: 15826113]
93. Hirsch LR, Stafford RJ, Bankson JA, Sershen SR, Rivera B, Price RE, Hazle JD, Halas NJ, West JL. Proc. Natl. Acad. Sci. 2003; 100:13549–13554. [PubMed: 14597719]
94. O'Neal DP, Hirsch LR, Halas NJ, Payne JD, West JL. Cancer Lett. 2004; 209:171–176. [PubMed: 15159019]
95. Schwartz JA, Price RE, Gill-Sharp KL, Sang KL, Khorchani J, Goodwin BS, Payne JD. Lasers Surg. Med. 2011; 43:213–220. [PubMed: 21412805]
96. Dong W, Li Y, Niu D, Ma Z, Gu J, Chen Y, Zhao W, Liu X, Liu C, Shi J. Adv. Mater. 2011; 23:5392–5397. [PubMed: 21997882]
97. Brevet D, et al. Chem. Commun. 2009:1475–1477.
98. Gary-Bobo M, et al. Angew. Chem. 2011; 123:11627–11631.
99. Kim S, Ohulchanskyy TY, Pudavar HE, Pandey RK, Prasad PN. J. Am. Chem. Soc. 2007; 129:2669–2675. [PubMed: 17288423]
100. Huang P, et al. Biomaterials. 2011; 32:9796–9809. [PubMed: 21917309]
101. Xu W, Luo T, Li P, Zhou C, Cui D, Pang B, Ren Q, Fu S. Int. J. Nanomed. 2012; 7:915.
102. Fan W, et al. J. Am. Chem. Soc. 2013; 135:6494–6503. [PubMed: 23574400]
103. Xiao Q, et al. J. Am. Chem. Soc. 2013; 135:13041–13048. [PubMed: 23924214]
104. Chen Y, et al. Angew. Chem. 2011; 123:12713–12717.

NIH-PA Author Manuscript

NIH-PA Author Manuscript

NIH-PA Author Manuscript

105. Wang X, Chen H, Zheng Y, Ma M, Chen Y, Zhang K, Zeng D, Shi J. Biomaterials. 2013; 34:2057–2068. [PubMed: 23246067]
106. Liberman A, Wu Z, Barback CV, Viveros R, Wang J, Ellies LG, Mattrey RF, Trogler WC, Kummel AC, Blair SL. J. Surg. Res. 2014
107. Martín-Saavedra FM, Ruíz-Hernández E, Boré A, Arcos D, Vallet-Regí M, Vilaboa N. Acta Biomater. 2010; 6:4522–4531. [PubMed: 20601238]
108. Renard P-EL, Buchegger F, Petri-Fink A, Bosnian F, Rüfenacht D, Hofmann H, Doelker E, Jordan O. Int. J. Hyperth. 2009; 25:229–239.
109. Le Renard P-E, Jordan O, Faes A, Petri-Fink A, Hofmann H, Rüfenacht D, Bosnian F, Buchegger F, Doelker E. Biomaterials. 2010; 31:691–705. [PubMed: 19878991]
110. Villanueva A, dela Presa P, Alonso JM, Rueda T, Martinez A, Crespo P, Morales MP, Gonzalez-Fernandez MA, Valdés J, Rivero G. J. Phys. Chem. 2010; C114:1976–1981.
111. Kaman O, Pollert E, Veverka P, Veverka M, Hadová E, Knížek K, Maryško M, Kašpar P, Klementová M, Grünwaldová V. Nanotechnology. 2009; 20:275610. [PubMed: 19531865]
112. Uskoković V, Košak A, Drofenik M. Mater. Lett. 2006; 60:2620–2622.
113. Wu SY-H, Yang K-C, Tseng C-L, Chen J-C, Lin F-H. J. Nanopart. Res. 2011; 13:1139–1149.
114. Ruan J, Ji J, Song H, Qian Q, Wang K, Wang C, Cui D. Nanoscale Res. Lett. 2012; 7:1–12. [PubMed: 22214494]
115. Giri S, Trewyn BG, Stellmaker MP, Lin VSY. Angew. Chem. Int. Ed. Engl. 2005; 44:5038–5044. [PubMed: 16038000]
116. Yang Q, Wang S, Fan P, Wang L, Di Y, Lin K, Xiao F-S. Chem. Mater. 2005; 17:5999–6003.
117. Porta F, Lamers GEM, Morrhayim J, Chatzopoulou A, Schaaf M, den Dulk H, Backendorf C, Zink JI, Kros A. Adv. Healthc. Mater. 2013; 2:281–286. [PubMed: 23184490]
118. Patel K, Angelos S, Dichtel WR, Coskun A, Yang Y-W, Zink JI, Stoddart JF. J. Am. Chem. Soc. 2008; 130:2382–2383. [PubMed: 18232687]
119. Zhao Y, Trewyn BG, Slowing II, Lin VSY. J. Am. Chem. Soc. 2009; 131:8398–8400. [PubMed: 19476380]
120. Fang W, Yang J, Gong J, Zheng N. Adv. Funct. Mater. 2012; 22:842–848.
121. Kong SD, Zhang W, Lee JH, Brammer K, Lal R, Karin M, Jin S. Nano Lett. 2010; 10:5088–5092. [PubMed: 21038917]
122. Kong SD, Lee J, Ramachandran S, Eliceiri BP, Shubayev VI, Lal R, Jin S. J. Control. Release. 2012; 164:49–57. [PubMed: 23063548]
123. Aznar E, Marcos MD, Martinez-Máñez RN, Sancenón FL, Soto J, Amorós P, Guillem C. J. Am. Chem. Soc. 2009; 131:6833–6843. [PubMed: 19402643]
124. Kim HJ, Matsuda H, Zhou H, Honma I. Adv. Mater. 2006; 18:3083–3088.

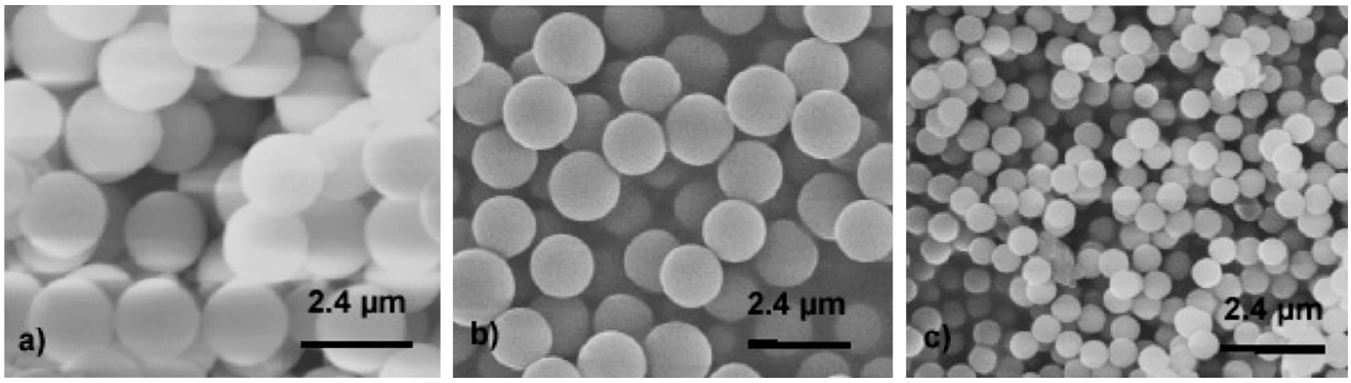

Fig. 1.

SEM images of solid silica nanoparticles synthesized by the Stöber method with varying rates of TEOS additions [3]: (a) rate of addition: 0.005 ml/min, (b) rate of addition: 0.05 ml/min and (c) rate of addition: 0.5 ml/min. Each order of magnitude increase in rate of TEOS addition resulted in a 33% decrease in particle size from ~ 1800 to 600 nm in diameter.

NIH-PA Author Manuscript
NIH-PA Author Manuscript
NIH-PA Author Manuscript

NIH-PA Author Manuscript
NIH-PA Author Manuscript
NIH-PA Author Manuscript

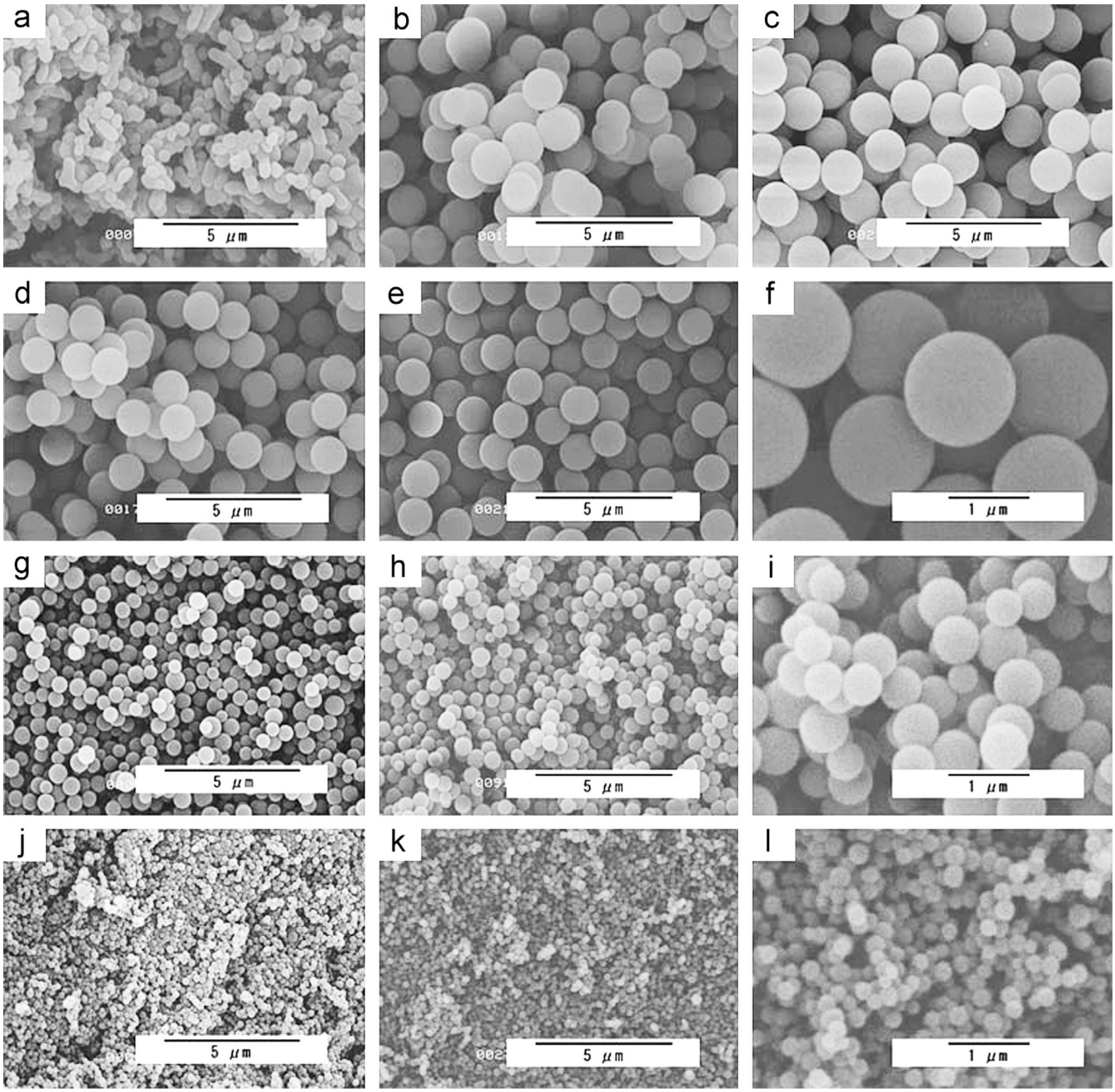

Fig. 2.

Silica nanoparticles synthesized by the Stöber method with variable methanol/TEOS ratios before and after calcination [6]. The MeOH/TEOS synthesis ratios and calcined *vs.* noncalcined status are as follows: (a) 300/noncalcined, (b) 750/noncalcined, (c) 1125/noncalcined, (d) 1500/noncalcined, (e) and (f) 1500/calcined, (g) 2250/noncalcined, (h) and (i) 2250/calcined, (j) 3000/noncalcined, and (k) and (1) 3000/calcined. As the ratio of methanol/TEOS increased from 300 to 1125, the particle size increased. However, from 1125 to 6000, the particle size decreased from 1500 nm to 10 nm in diameter.

NIH-PA Author Manuscript

NIH-PA Author Manuscript

NIH-PA Author Manuscript

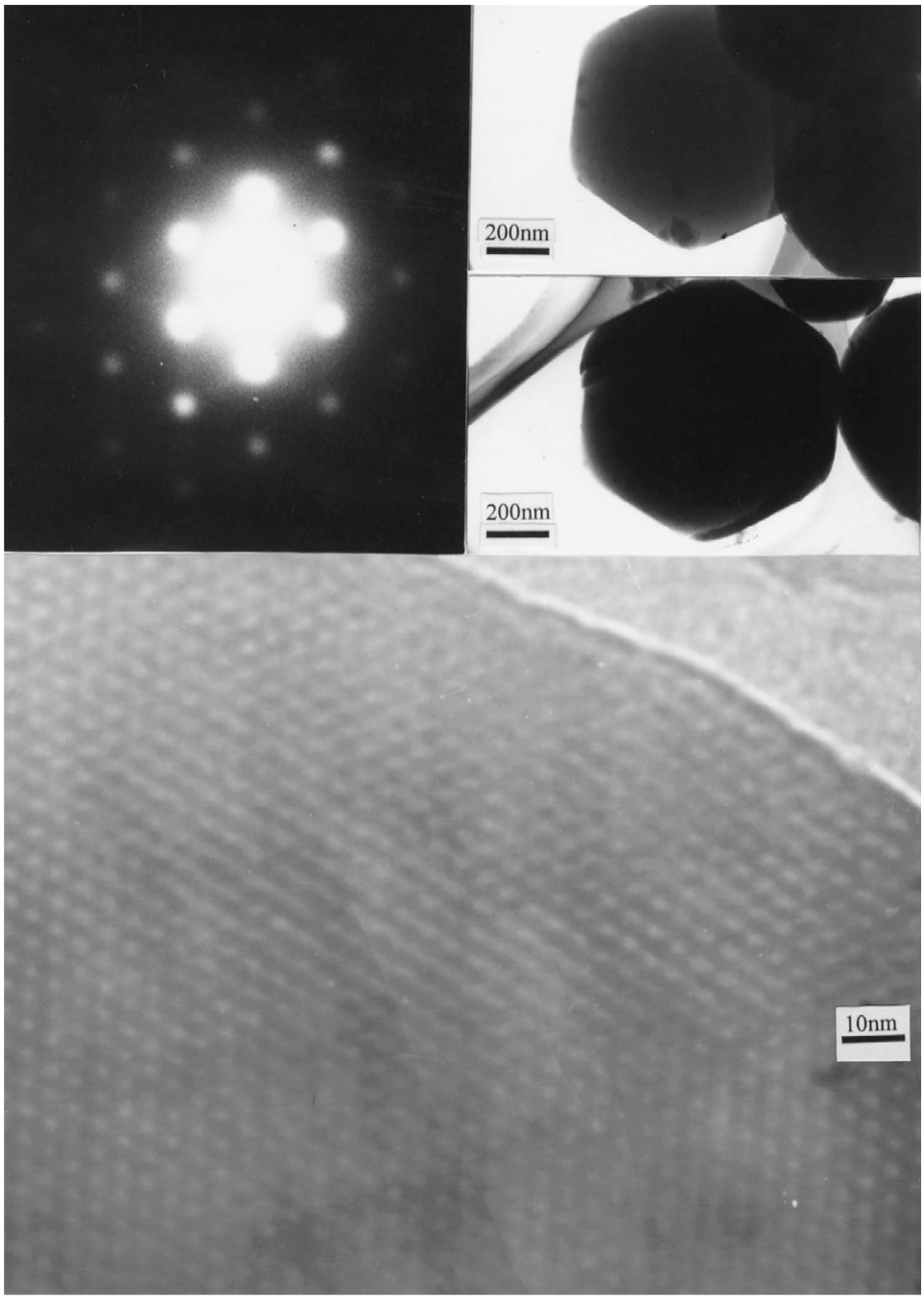

Fig. 3.

Analysis of mesoporous particles by transmission electron microscopy [8]. Top left image is the electron diffraction pattern of the mesoporous particles clearly displaying a hexagonal pore structure. Top right images are low magnification TEM images. Bottom image is high magnification TEM showing the highly ordered pore structure of the particles.

NIH-PA Author Manuscript
NIH-PA Author Manuscript
NIH-PA Author Manuscript

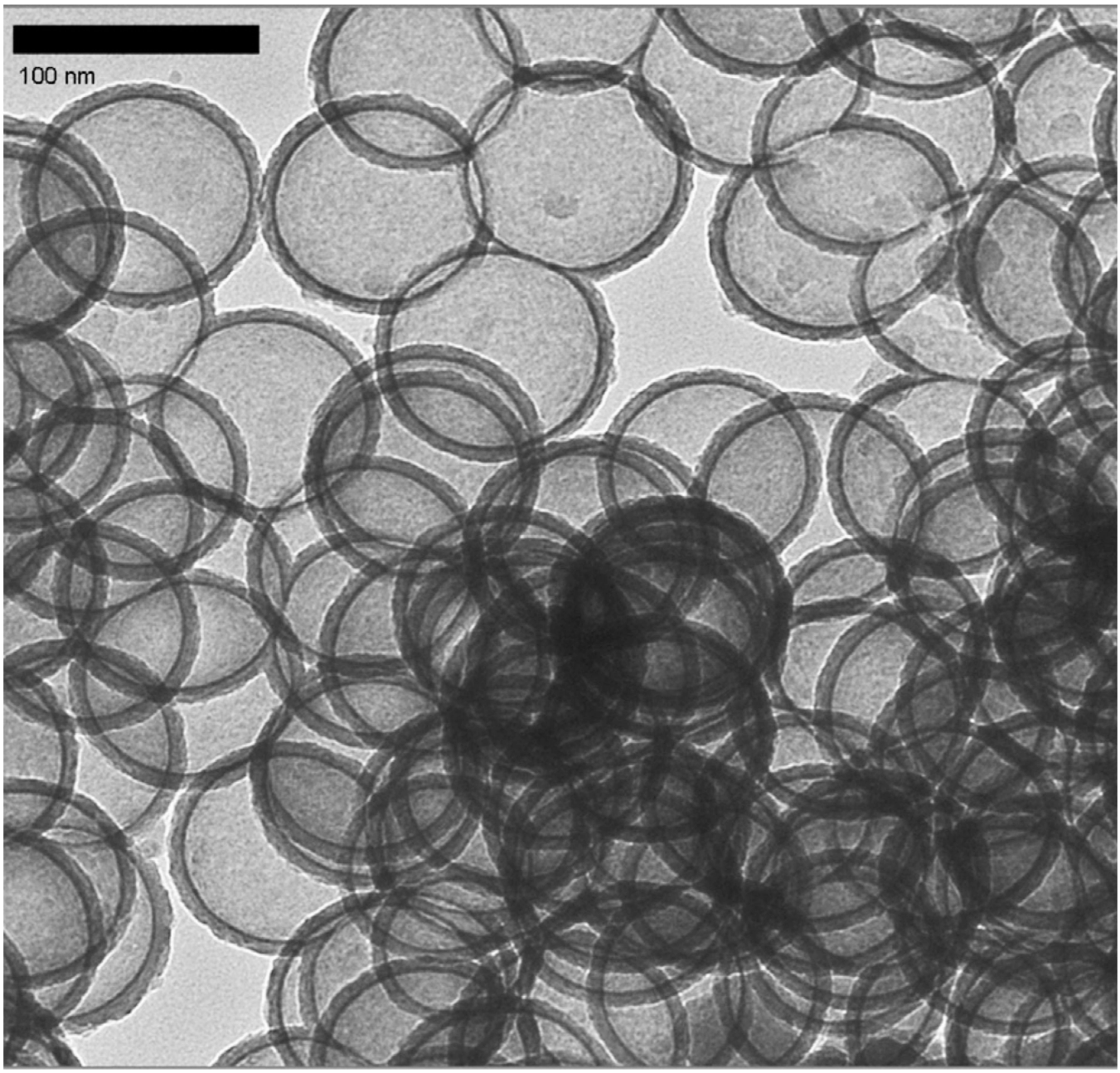

Fig. 4.

Transmission eletron microscopy of calcined 100 nm hollow silica nanoparticles synthesized from polystyrene templates [22]. Due to the commercial template used for synthesis, the resulting nanoshells are highly uniform with a shell thickness of 10 nm. Scale bar is 100 nm.

NIH-PA Author Manuscript
NIH-PA Author Manuscript
NIH-PA Author Manuscript

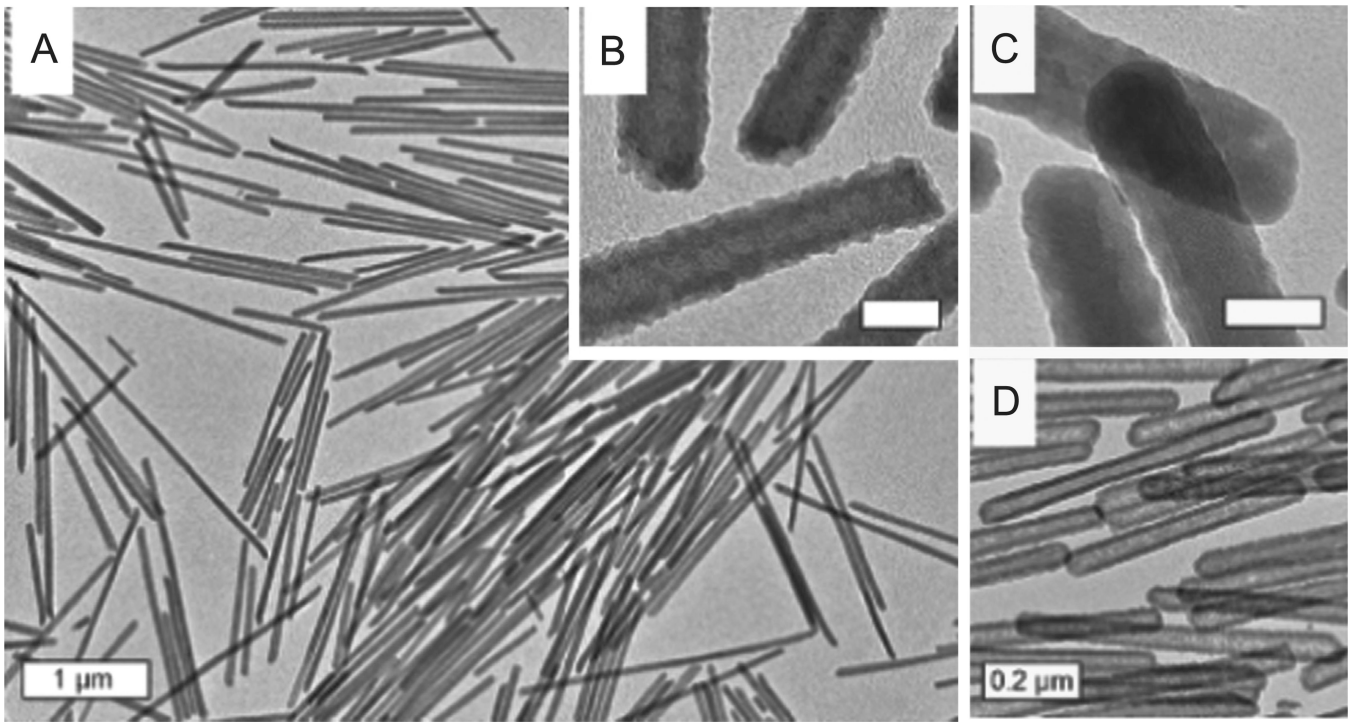

Fig. 5.

Transmission electron microscopy of the various shaped silica nanoparticles templated onto metal organic framework tempaltes [26]: (A) and (B) Polyvinylpyrrolidone functionalized MOF with a 2–3 nm layer of silica. (C) Polyvinylpyrrolidone functionalized MOF with a 8–9 nm layer of silica. (D) Hollow silica nanorod resulting from low pH treatment of polyvinylpyrrolidone functionalized MOF with a 8–9 nm layer of silica. Blank scale bars represent 50 nm.

NIH-PA Author Manuscript

NIH-PA Author Manuscript

NIH-PA Author Manuscript

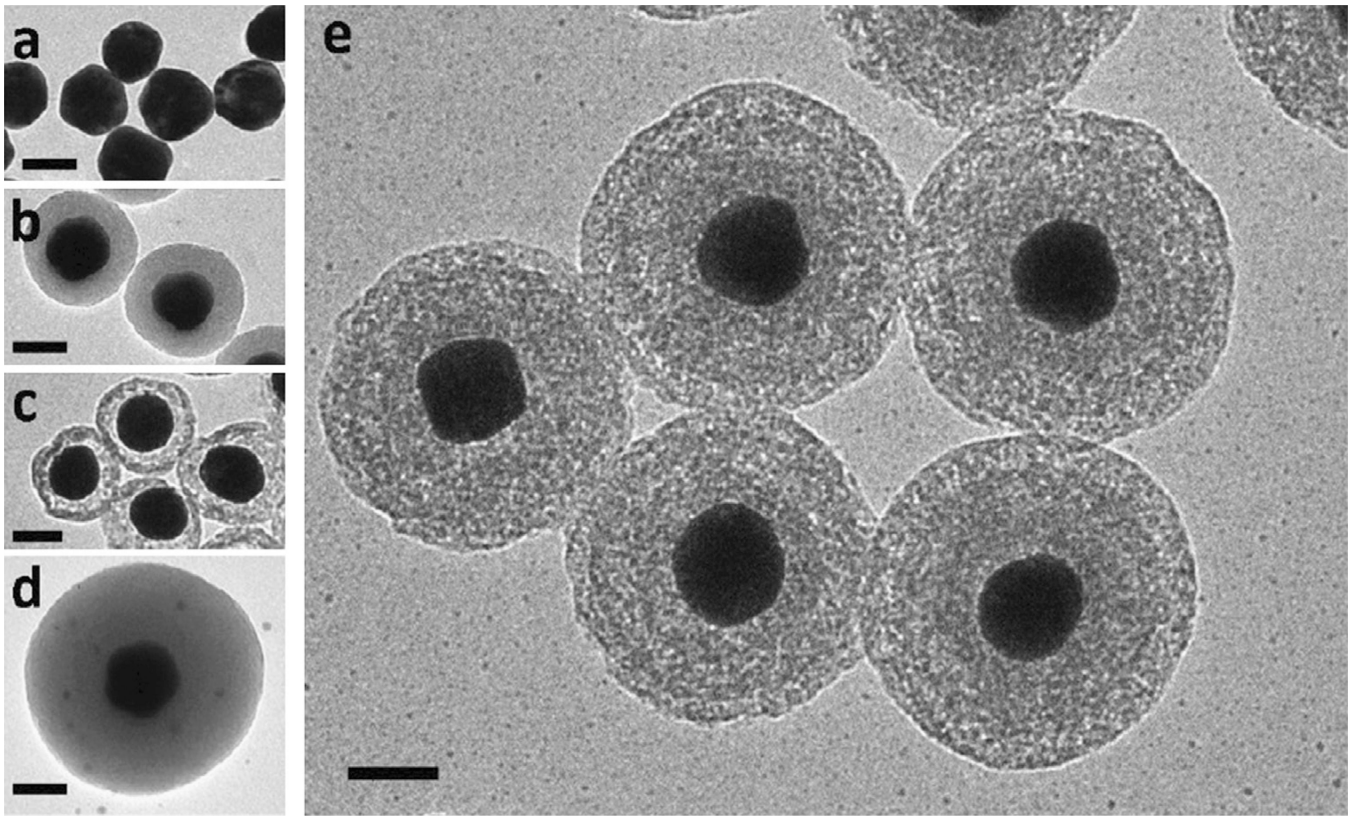

Fig. 6.

TEM images of stepwise synthesis of yolk–shell and multi–shell Au-core–silica nanoparticles [29]. (a) Au–core, (b) Au–core encapsulate in silica with the outer layer hardened with 2-propanol, (c) Au–core–silica yolk–shell particle after etching inner layer of silica, (d) multishell Au–core particle undergoing multiple steps of Stöber growth prior and 2-propanol treatment. (e) Multishell Au–core–silica particles after etching. Scale bar is 50 nm.

NIH-PA Author Manuscript

NIH-PA Author Manuscript

NIH-PA Author Manuscript

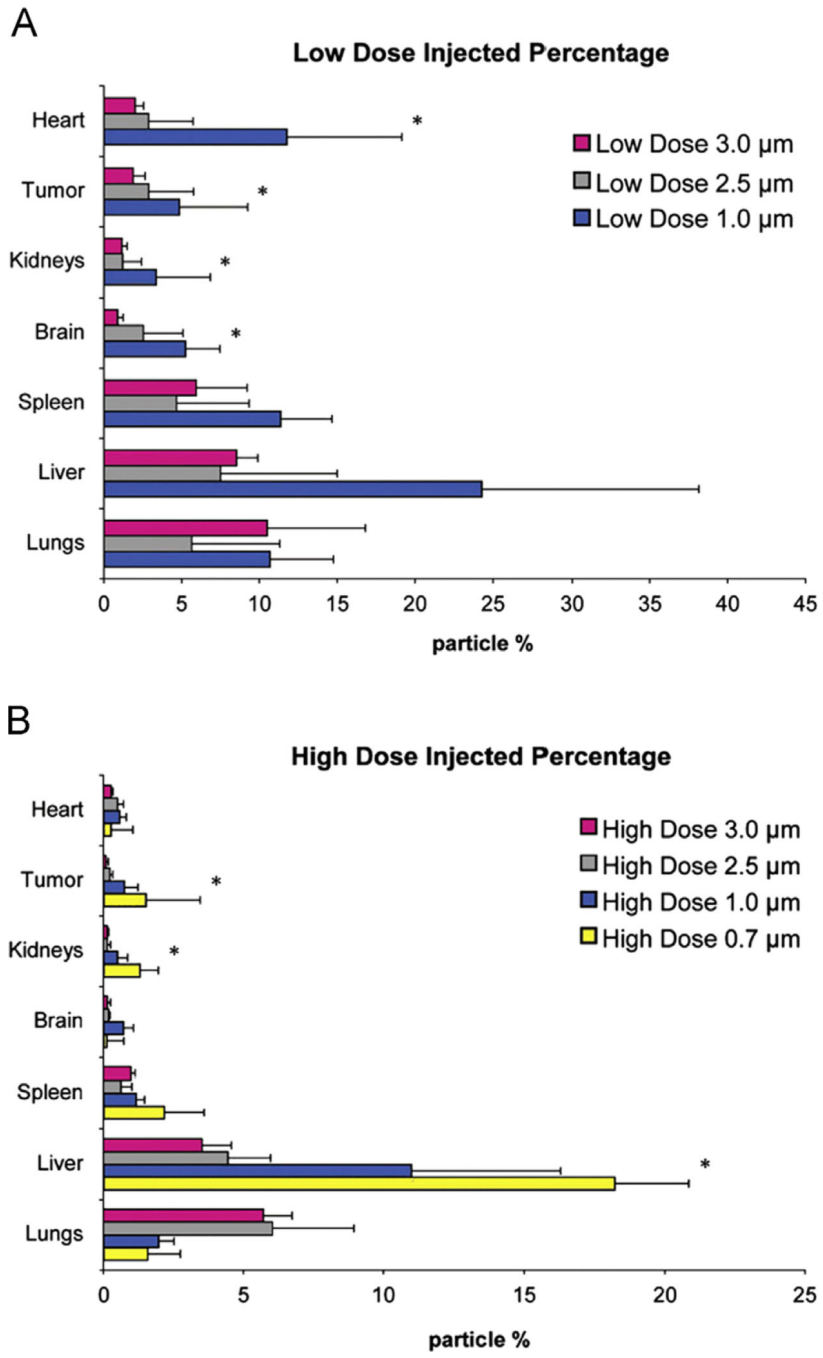

Fig. 7.

Biodistribution of variably sized silica nanoparticles in MDA-MB-231 tumor bearing mice by ICP-AES [24]: (A) animals that received a low dose of particles (10^7 particles/animal) and (B) animals that received a high dose of particles (10^8 particles/animal). As the dose increased a factor of 10 ×, the accumulation of particles in all sizes increased primarily in RES organs.

NIH-PA Author Manuscript

NIH-PA Author Manuscript

NIH-PA Author Manuscript

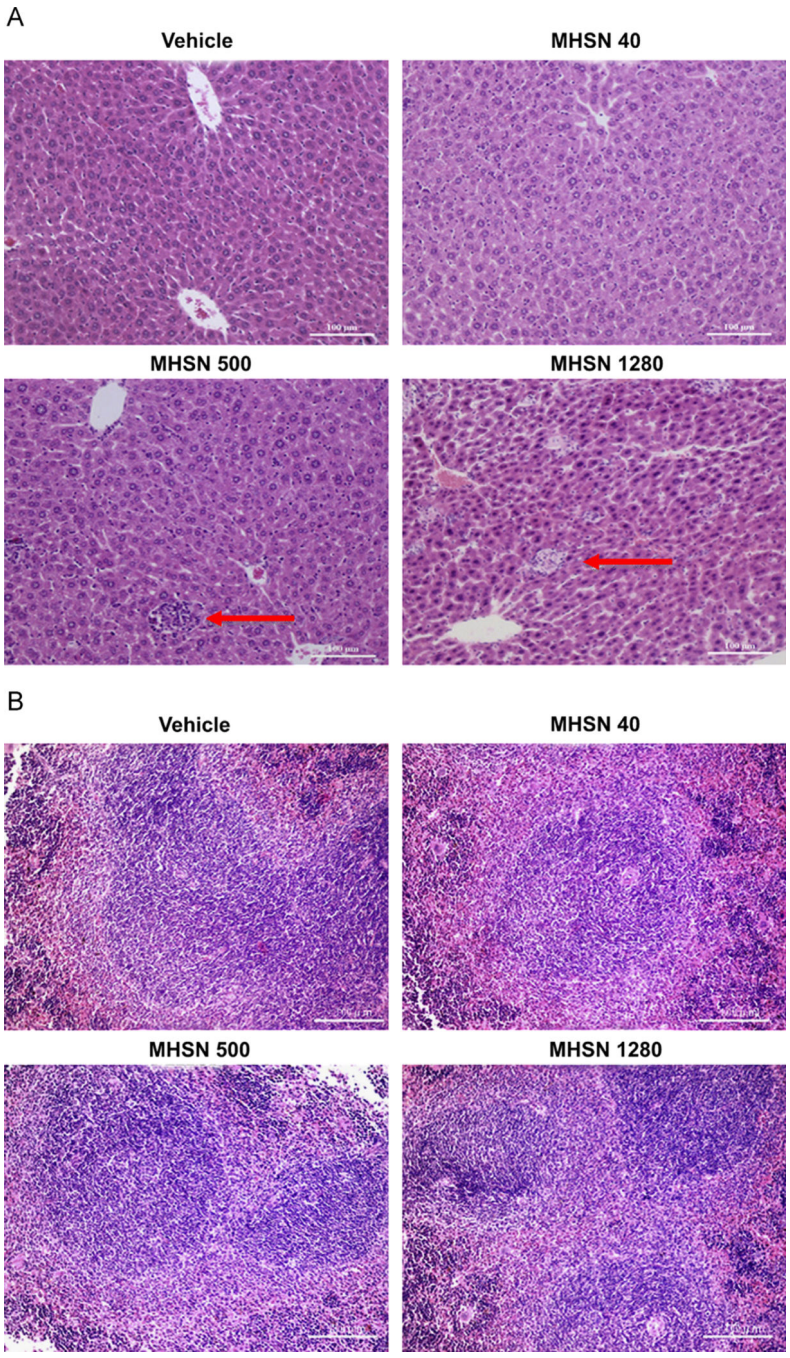

Fig. 8.

Histology of hematoxylin and eosin stained mouse liver and spleen after variable doses of mesoporous silica nanoparticles.[53]. Doses ranged from 0 to 1280 mg/kg: (A) liver tissues and (B) spleen tissues. Degenerative necrosis and microgranulation (red arrows) is observed in liver tissues in doses exceeding 500 mg/kg. Scale bar is 100 μm.

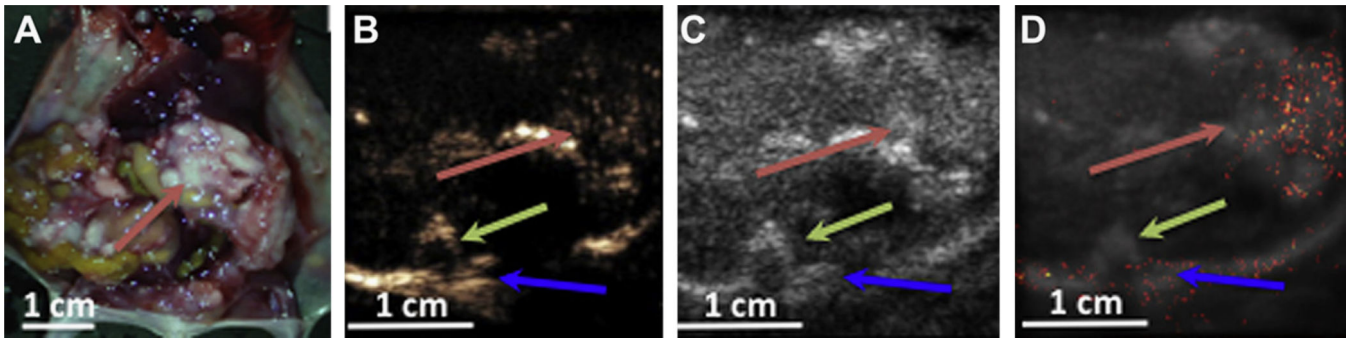

Fig. 9.

2 μm silica shells injected IP into IGROV-1 ovarian tumor bearing nu/nu mice. Red arrows in all images point to the tumor, the green arrows are the backbone of the mouse, and the blue arrows point to the bottom of the mouse [61]: (A) post mortem examination of mouse reveals large white IGROV-1 tumor mass in the peritoneum. (B) Contrast pulse sequencing (CPS) imaging of the mouse tumor, some particle dependent signal can be seen in the tumor mass. (C) B-mode imaging of the mouse tumor. (D).Integrated heat map of contrast signal derived from CPS imaging overlayed on the B-mode imaging to accentuate the presence of silica shells in the tumor.

NIH-PA Author Manuscript
NIH-PA Author Manuscript
NIH-PA Author Manuscript

NIH-PA Author Manuscript

NIH-PA Author Manuscript

NIH-PA Author Manuscript

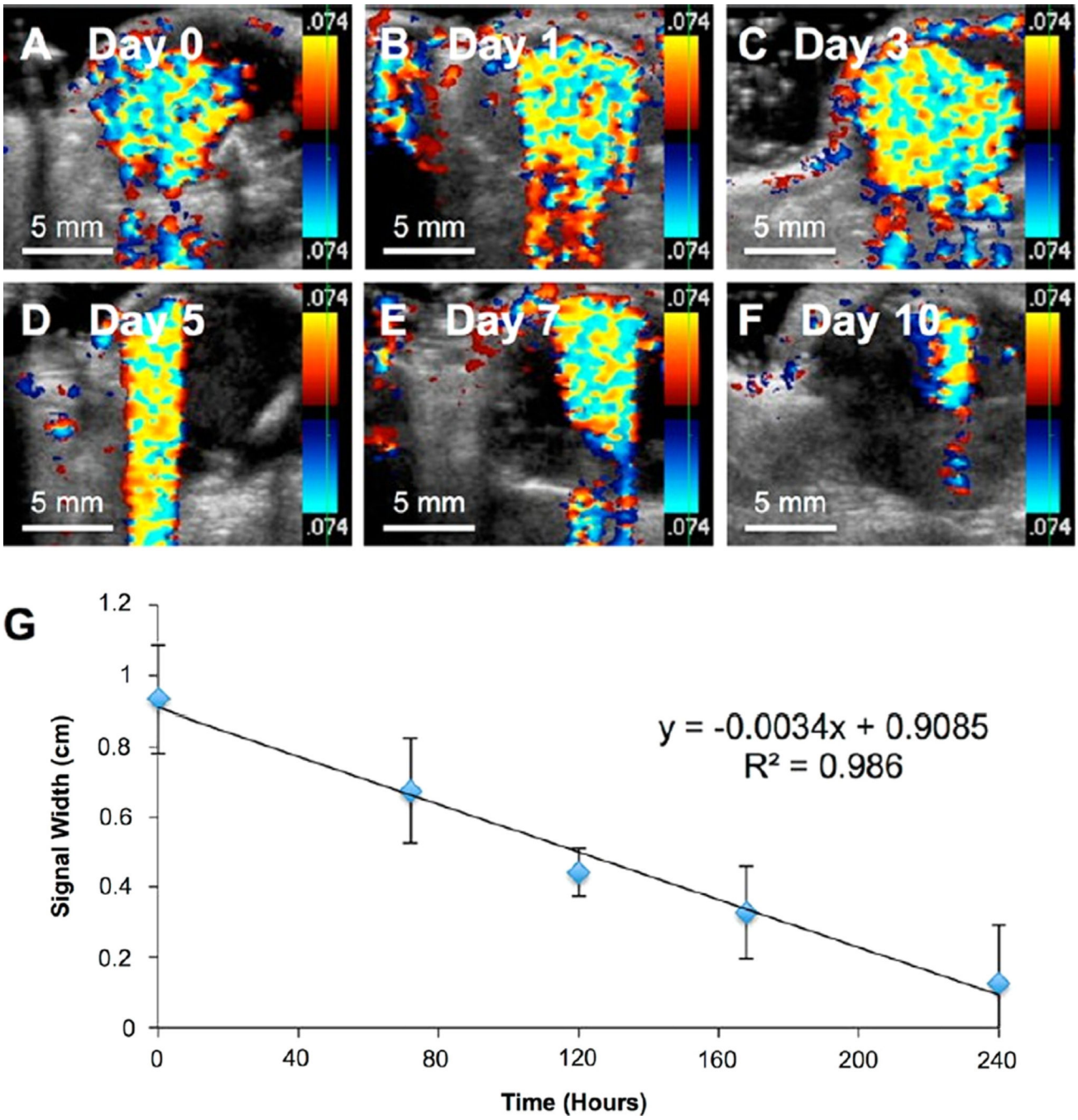

Fig. 10.

Intratumoral PFC filled iron-silica nanoshell imaging longevity [64]: (A–F) 50 μl of nanoshells were injected directly into Py8119 epithelial breast tumor bearing nu/nu mice and imaged by color Doppler ultrasound intermittenly over 10 days. (G) Color Doppler signal width was plotted against time to show a linear decay of signal over the course of 10 days.

NIH-PA Author Manuscript
NIH-PA Author Manuscript
NIH-PA Author Manuscript

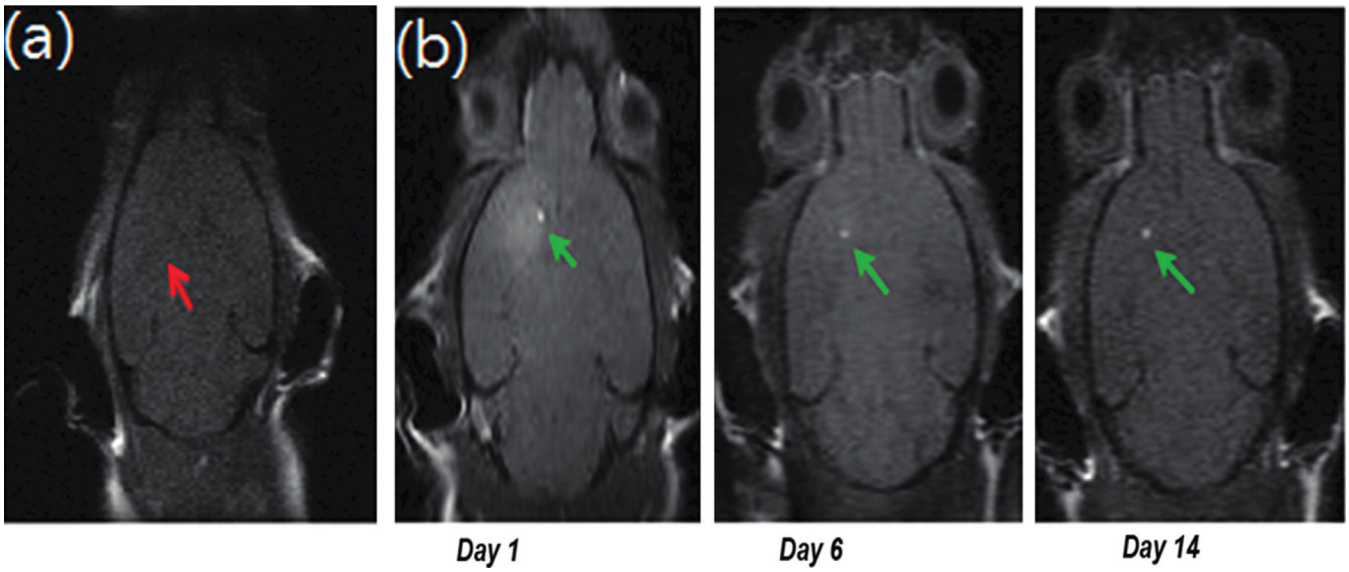

Fig. 11.

MRI cross section of mouse brain with transplanted mesenchymal stem cells loaded with manganese oxide loaded mesoporous silica nanoparticles [80]: (a) Control MSCs into mice with no manganese oxide show no signal under MRI as indicated by the red arrow. (b) Manganese oxide loaded silica particles incubated into the MSCs show strong MRI signal over the course of 14 days indicated by the green arrow.

NIH-PA Author Manuscript
NIH-PA Author Manuscript
NIH-PA Author Manuscript

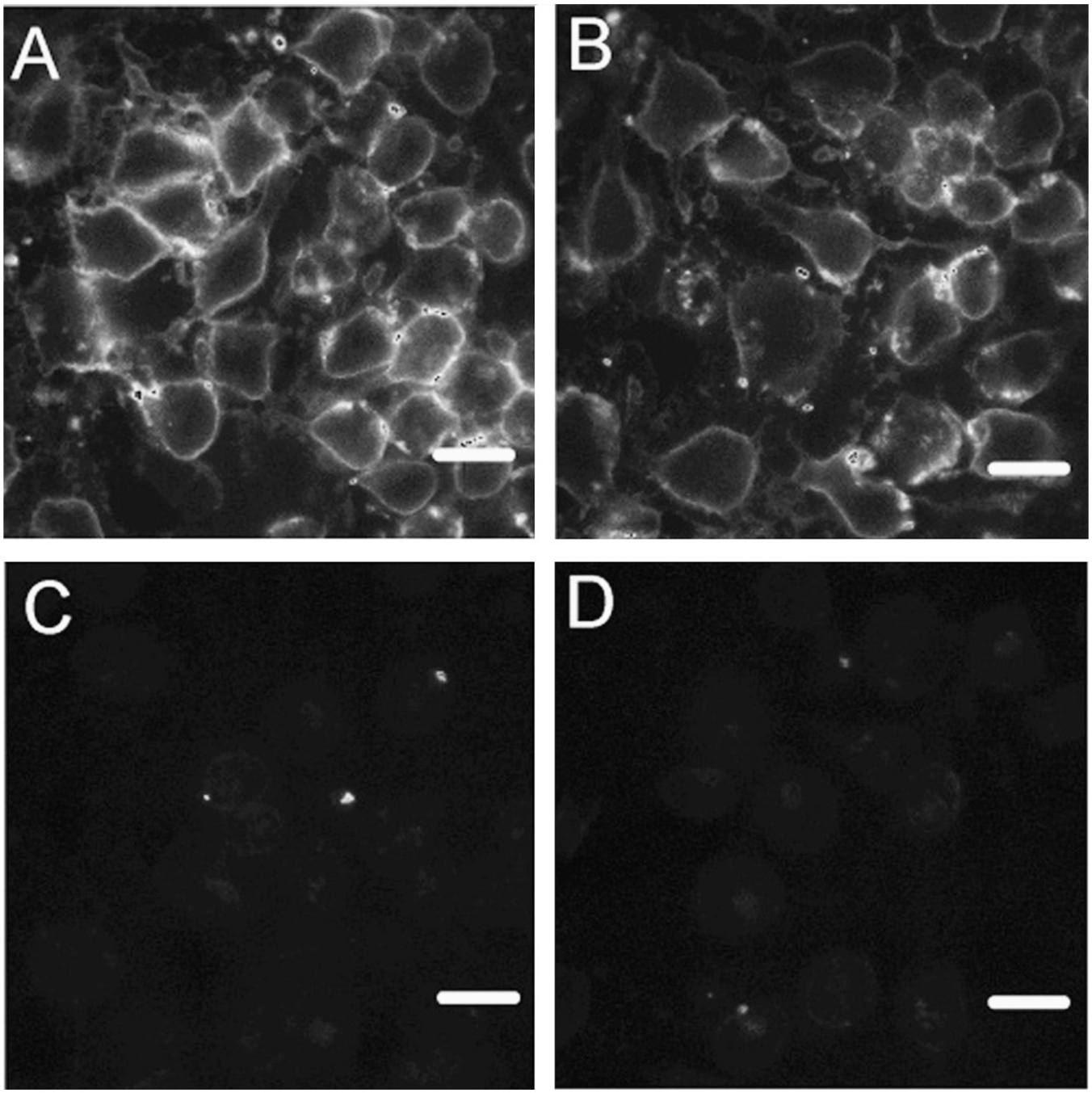

Fig. 12.

Fluorescent imaging of rat basophilic leukemia mast cells being labeled by silica nanoparticles [83]: (A) and (B) mast cell receptors labeled with IgE functionalized flourescent silica nanoparticles. (C) and (D) Competitive inhibition of FcεRI receptor with free IgE prevented nanoparticle labeling. Scale bar is 10 μm.

NIH-PA Author Manuscript
NIH-PA Author Manuscript
NIH-PA Author Manuscript

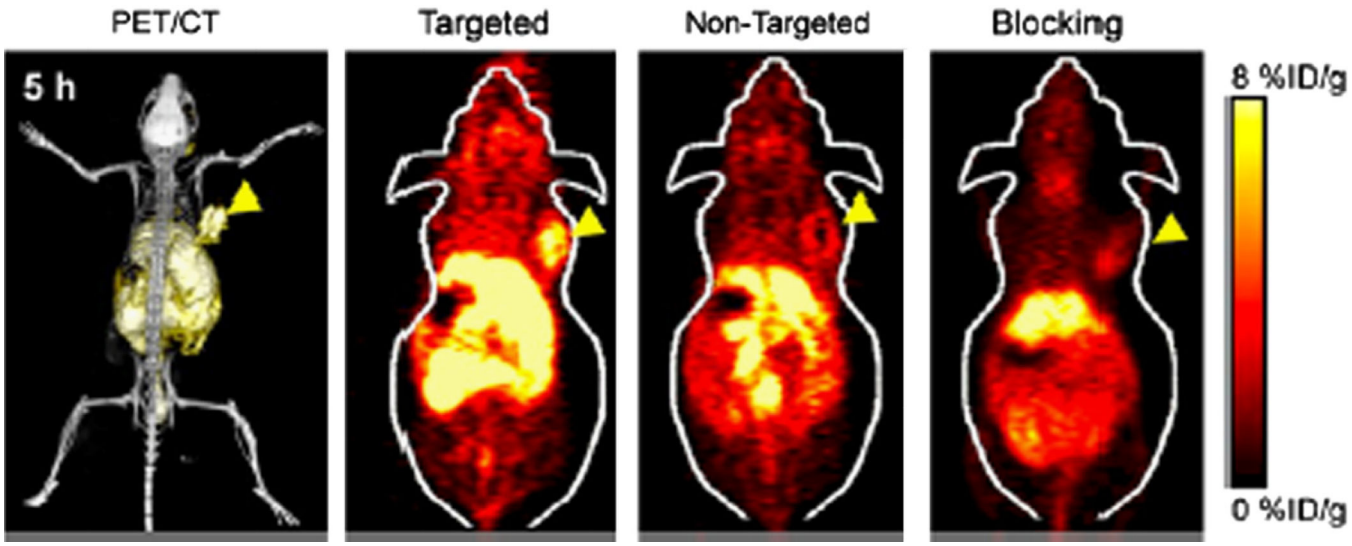

Fig. 13.

PET/CT and PET imaging of 4T1 tumor bearing mice 5 h after being dosed with Cu-NOTA-mesoporous silica nanoparticles [87]. The left image contains a PET/CT image to clearly demonstrate the location of the implanted 4T1 tumor also indicated by the yellow triangle in all images. Comparing the PET images, more TRC105 targeted particles are present in the tumor compared to non-targeted and inhibited particles.

NIH-PA Author Manuscript

NIH-PA Author Manuscript

NIH-PA Author Manuscript

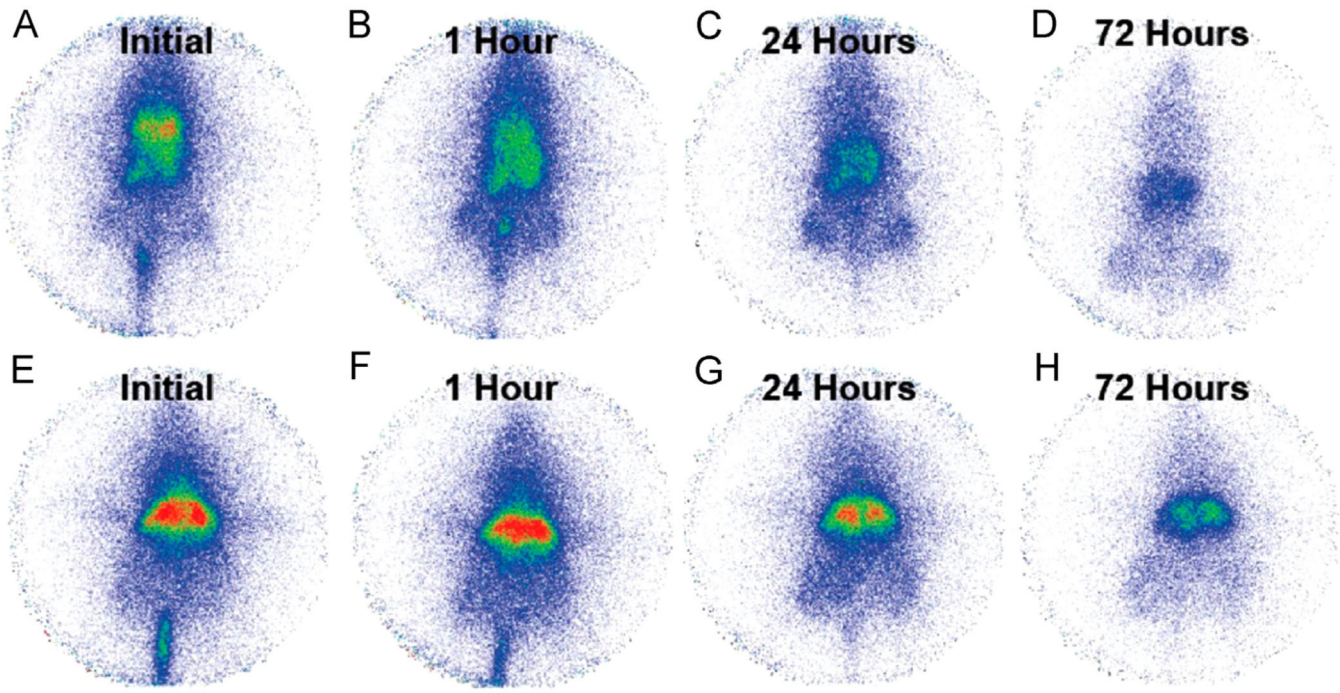

Fig. 14.

Gamma scinitigraphy of IV administered ^{111}In-DTPA–Fe–SiO_2 and pure SiO_2 nanoshells in Py8119 tumor bearing mice [56]: (A)–(D) Gamma scinitigraphy of ^{111}In-DTPA–Fe–SiO_2 over the course of 72 h. (E)–(H) Gamma scinitigraphy of ^{111}In-DTPA–SiO_2 over the course of 72 h.

NIH-PA Author Manuscript

NIH-PA Author Manuscript

NIH-PA Author Manuscript

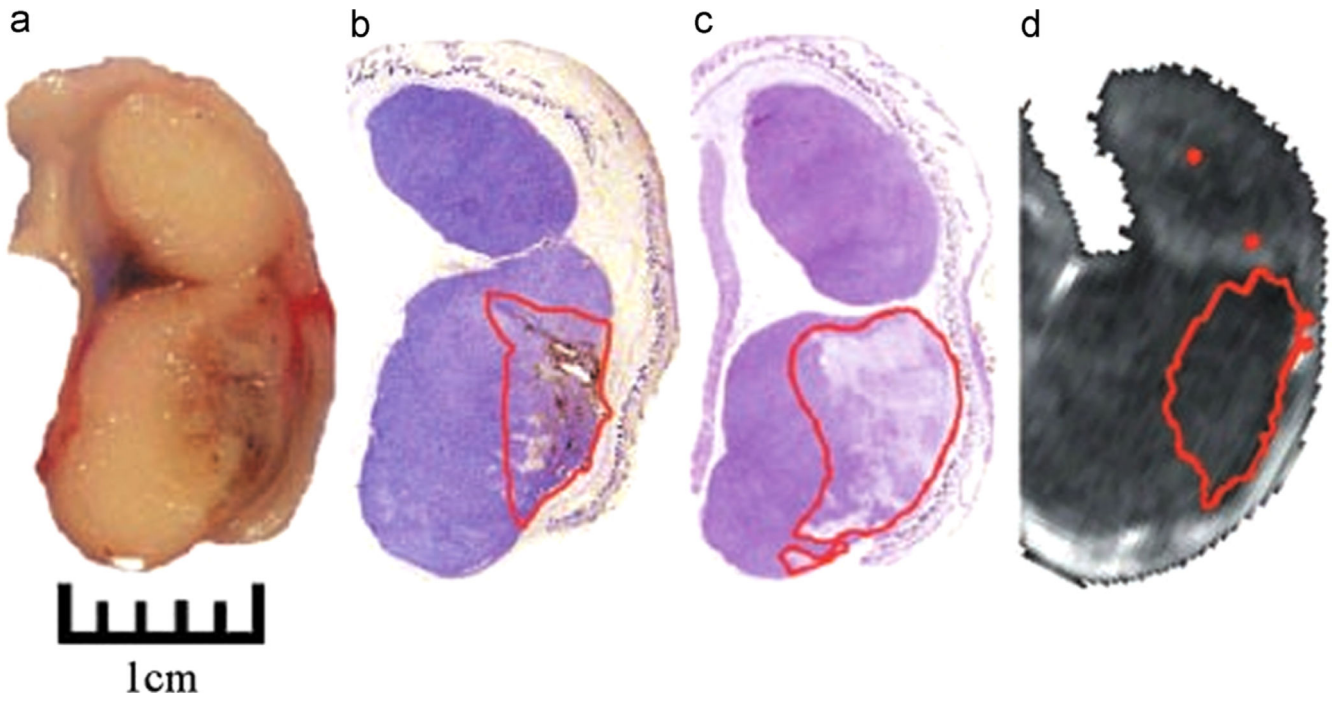

Fig. 15.

Examination of venereal tumor in SCID/j mice after photothermal irradiation with intratumorally administered Fe_3O_4–Au silica nanoparticles [93]: (a) Gross examination reveals a region of discolored damaged tissue on the lower right region of the tissue. (b) Silver staining was applied to the sectioned tissue to determine the location of the particles which are outlined in red. (c) H&E staining of the tissue reveals that the damaged tissue outlined in red overlaps with the location of the particles. (d) Magnetic resonance thermal imaging also displays a region of thermal damage overlapping in the region of the particles.

NIH-PA Author Manuscript

NIH-PA Author Manuscript

NIH-PA Author Manuscript

Fig. 16.

Photodynamic therapy with two-photon excitation of photosensitizer loaded mesoporous silica nanoparticles in HCT-116 tumor bearing mice 30 days after treatment [98]. The top row is control tumors with no treatment or particles (*n*=3). The middle row received the photosensitizer loaded mesoporous silica nanoparticles but no photodynamic irradiation (*n*=4). The bottom row received both particles and irradiation (*n*=4). All the samples in each group are shown from left to right. Scale bars are 2 cm.

NIH-PA Author Manuscript
NIH-PA Author Manuscript
NIH-PA Author Manuscript

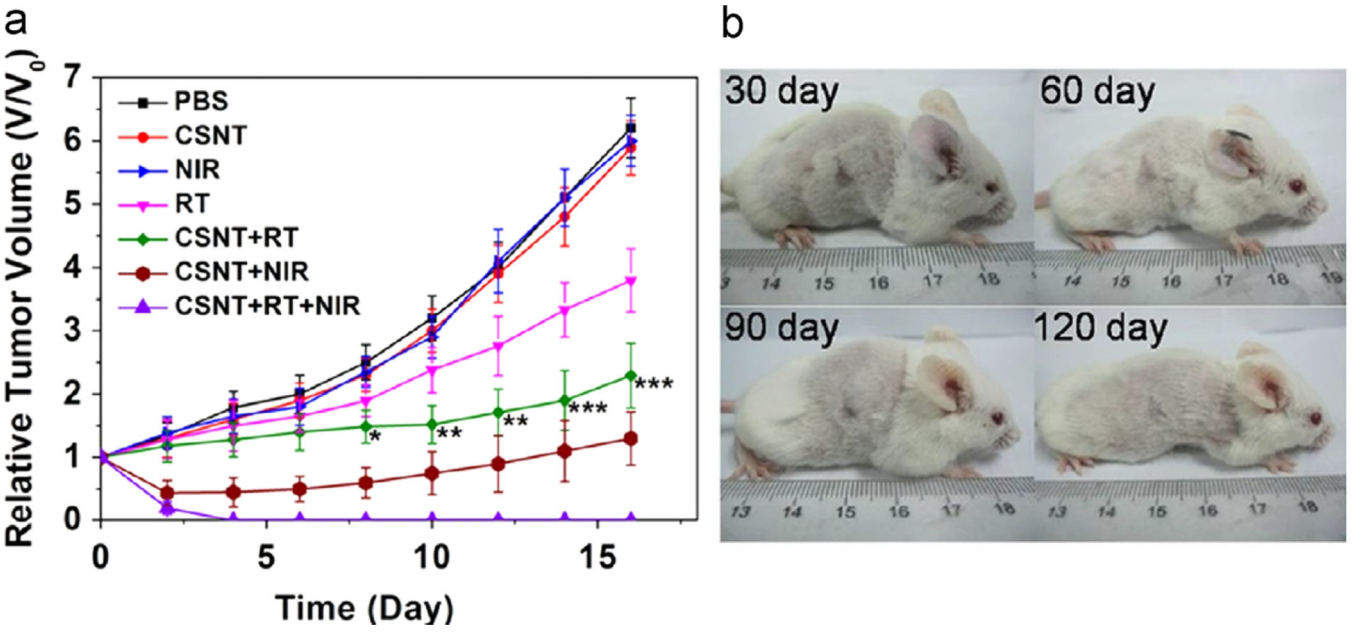

Fig. 17.

In vivo analysis of 4T1 murine breast tumor response to CSNT (rare earth core-silica shelled-CuS functionaled nanoparticles) in combination with X-ray radiotherapy and near IR irradiation [103]. ~200 μg of particles were injected intratumorally; NIR was applied at 980 nm with a power of 1.5 W/cm^2; radiotherapy was applied at 6 Gy: (a) relative tumor volume response over time with CSNT and/or NIR treatment/X-ray radiotherapy and (b) mouse observation from group which received CSNT+RT+NIR over the course or 120 days post treatment. No tumor growth/recurrence is observed.

NIH-PA Author Manuscript

NIH-PA Author Manuscript

NIH-PA Author Manuscript

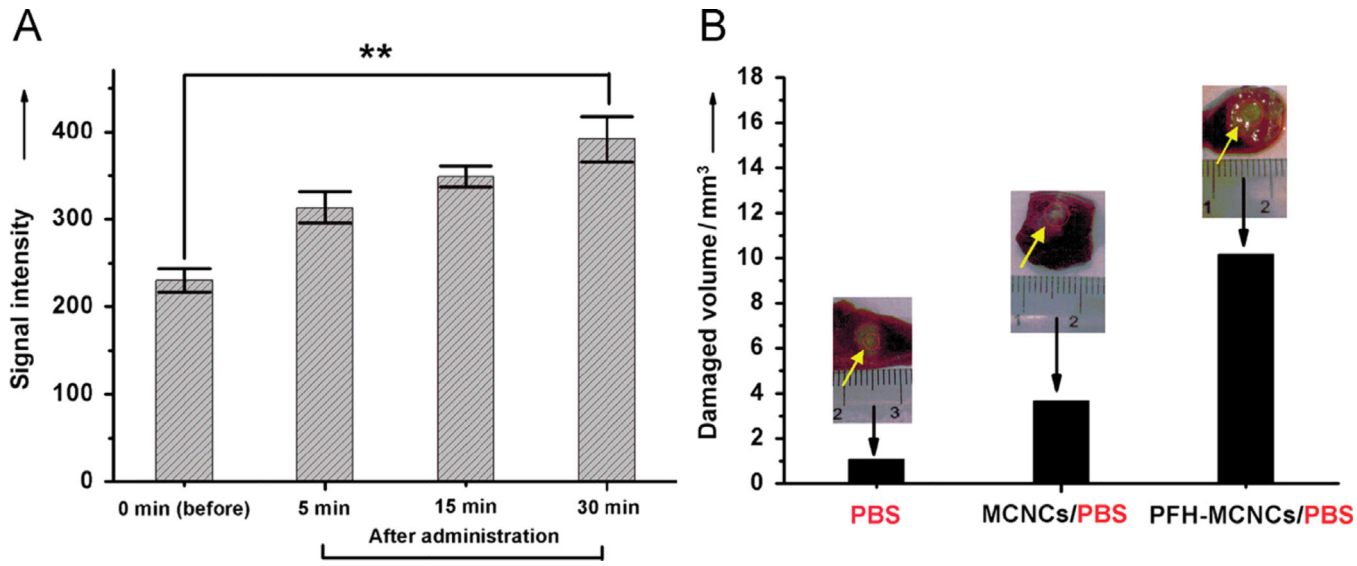

Fig. 18.

IV administration of PFH filled MnO functionalized hollow mesoporous silica shells to VX2 tumor bearing rabbits [96]. (A) The MRI T1 signal in the tumor after nanoparticle administration is used to guide when HIFU should be administered. (B) Response to HIFU at 150 W for 5 s in the presence of no particles (PBS), non-loaded particles, and PFH loaded particles. The particles acoustically scatter allowing for increased themal deposition, which is enhanced when PFH is also present.

NIH-PA Author Manuscript

NIH-PA Author Manuscript

NIH-PA Author Manuscript

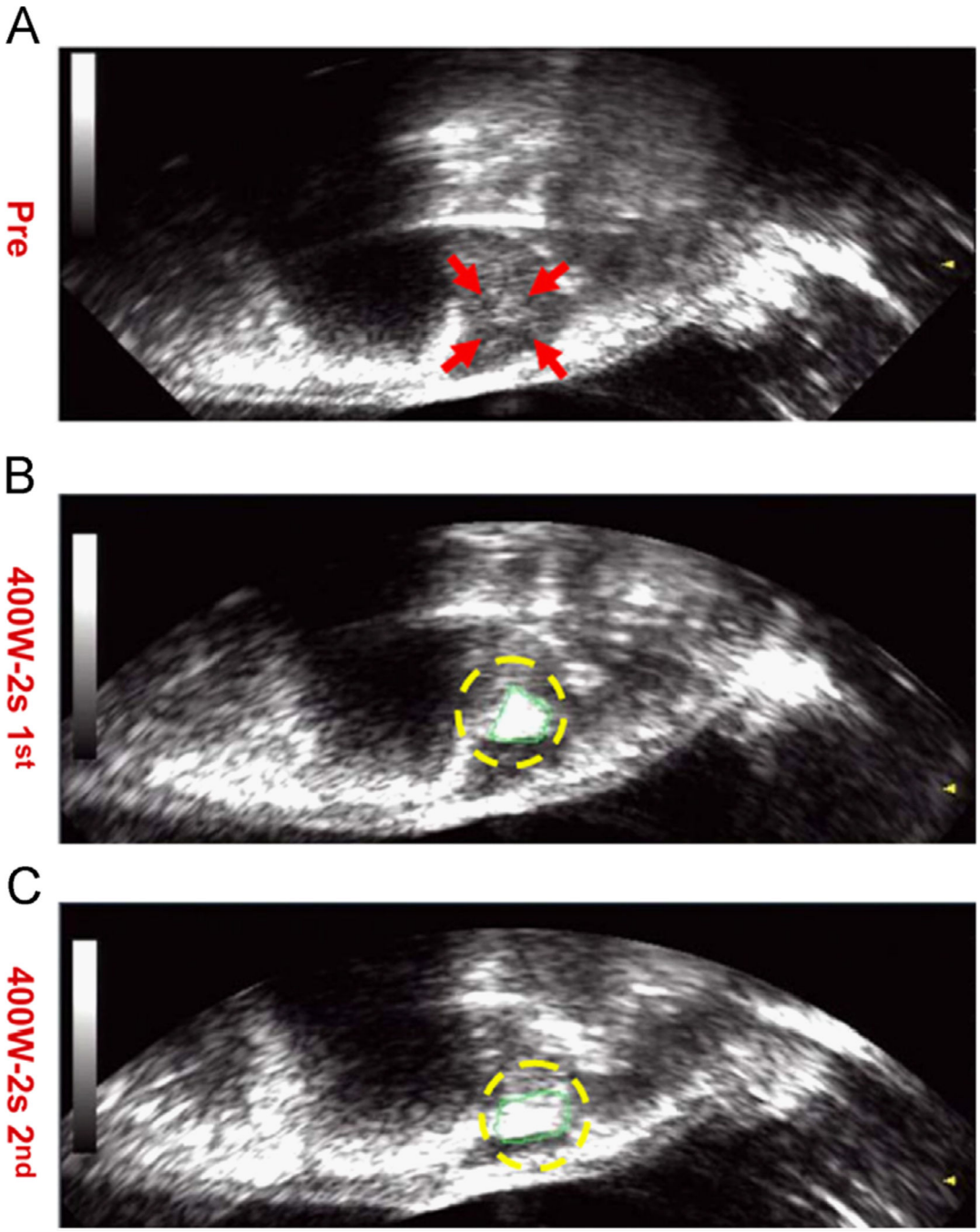

Fig. 19.

In vivo HIFU of PFH loaded Au–silica mesoporous particles in VX2 tumors in rabbit livers [105]. Particles were administered intravenously and allowed to circulate for 30 min; afterwards, HIFU was applied at 400 W for 2 s. Compred to pre-HIFU (A), each HIFU application ((B) and (C)) could be observed by an echogenic change in the tumor.

NIH-PA Author Manuscript
NIH-PA Author Manuscript
NIH-PA Author Manuscript

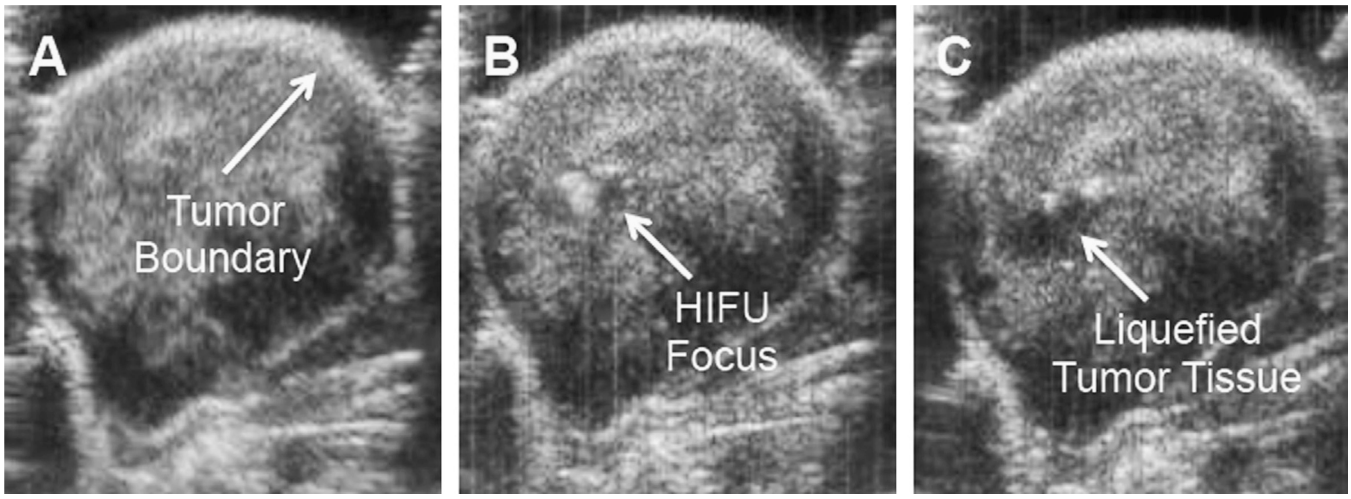

Fig. 20.

In vivo HIFU of PFP filled iron silica nanoshells in Py8119 tumors in nu/nu mice: (A) B-mode imagine before HIFU [106]. (B) Bubble cavitation is observed in the focal zone of the HIFU. (C) A black zone is present in the area of bubble cavitation which is filled with liquefied tissue.

NIH-PA Author Manuscript

NIH-PA Author Manuscript

NIH-PA Author Manuscript

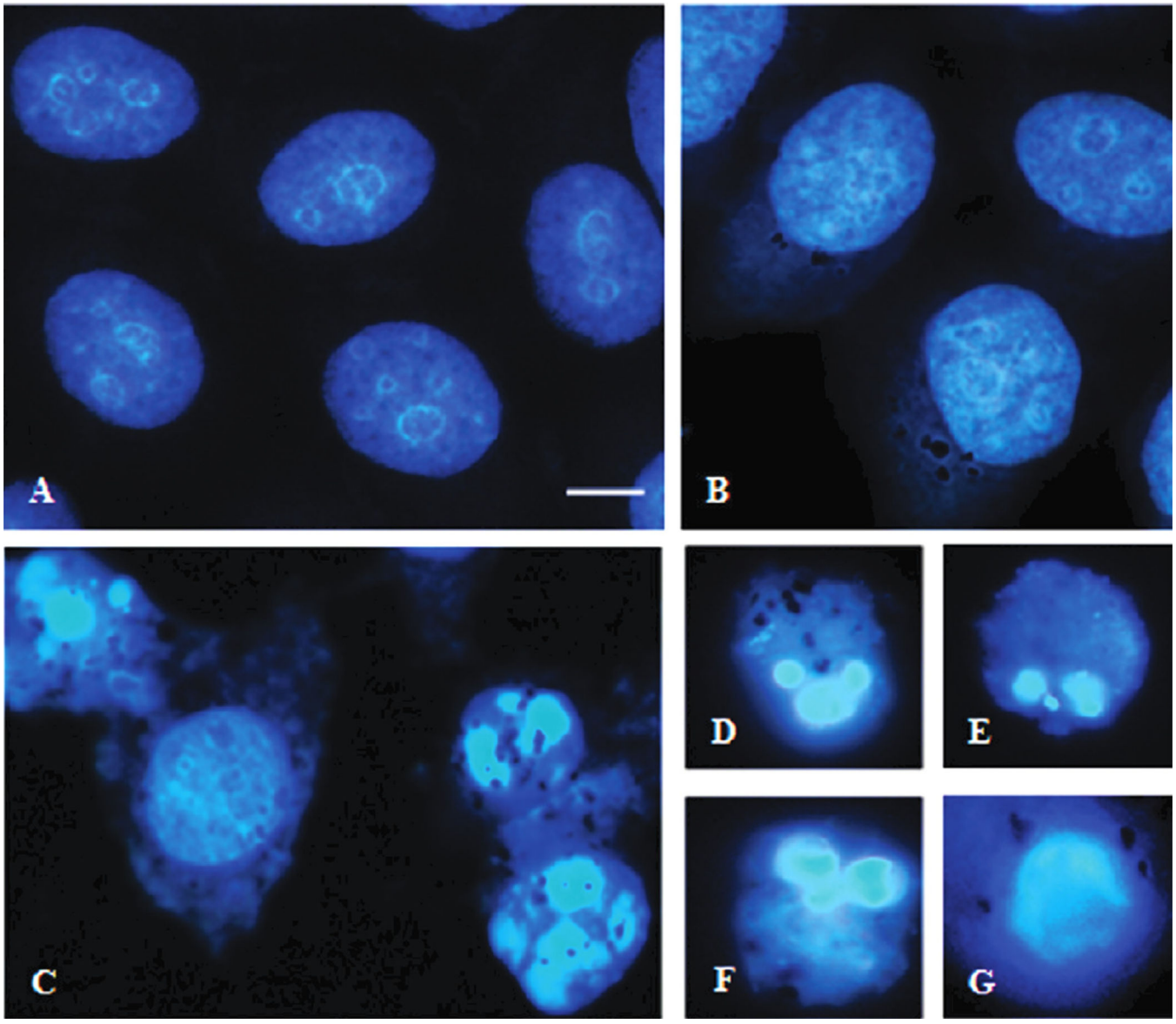

Fig. 21.

In vitro HeLa cell response to perovskite loaded silica particles and AMF. All cells stained with Hoechst 33258 [110]: (A) control cells with no particles or AMF, (B) control cells with particles and no AMF. (C)–(F) Cell deformation, detachment and death after incubation with particles and receiving AMF at 100 kHz and 15 mT for 30 min.

NIH-PA Author Manuscript
NIH-PA Author Manuscript
NIH-PA Author Manuscript

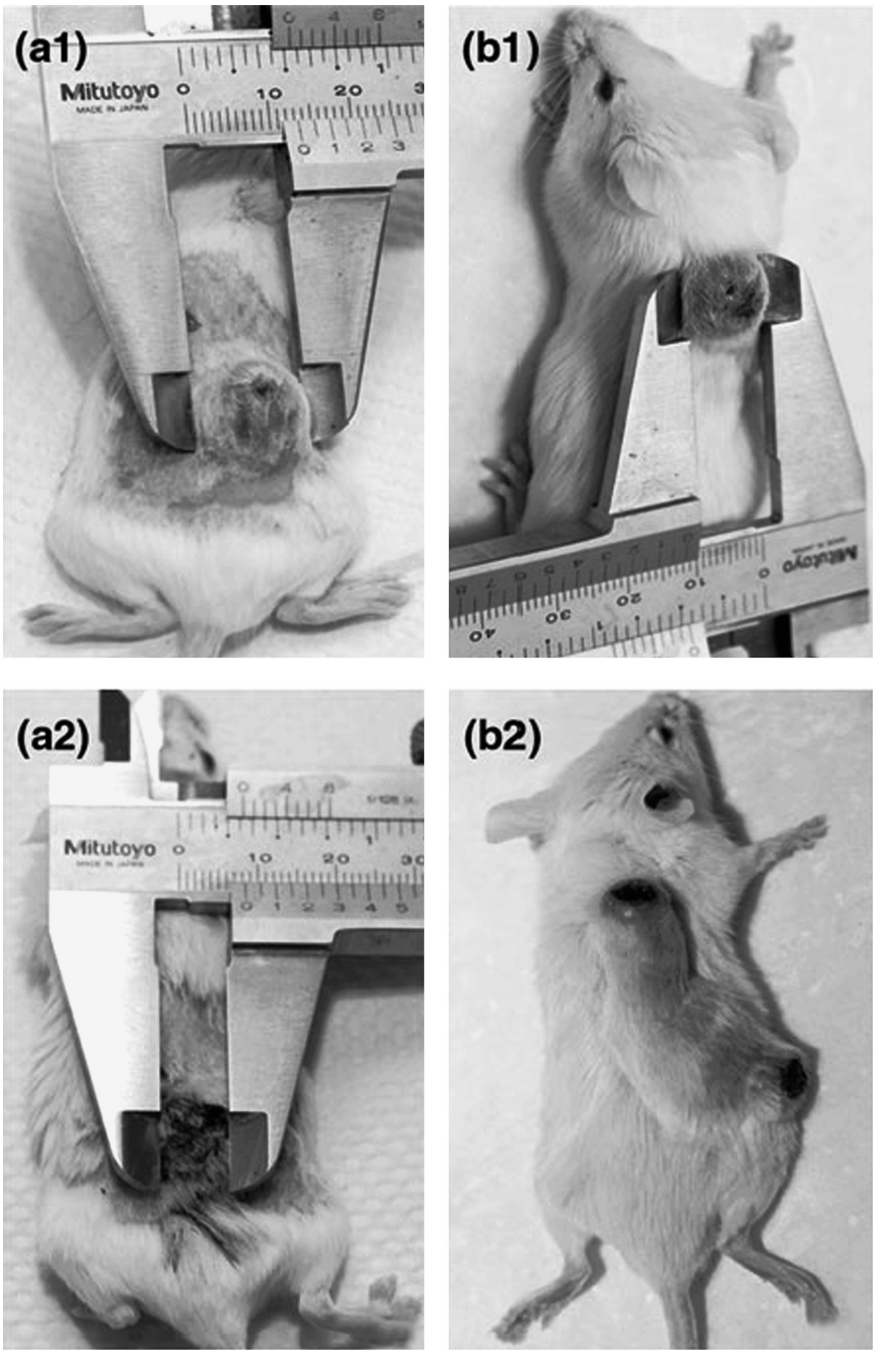

Fig. 22.

Hyperthermia with Fe–CaS–SiO_2 nanoparticles in CT-26 tumor bearing Balb/c mice. Both groups received exposure to AMF for 20 min at 750 kHz and 10 Oe [113]: (a1) initial tumor injected with magnetic nanoparticles. (a2) 15 days after initial treatment, tumor mass is replaced with a black scarred region. (b1) Initial control with no particles. (b2) Control mouse with rapid increase in tumor volume after 15 days.

NIH-PA Author Manuscript

NIH-PA Author Manuscript

NIH-PA Author Manuscript

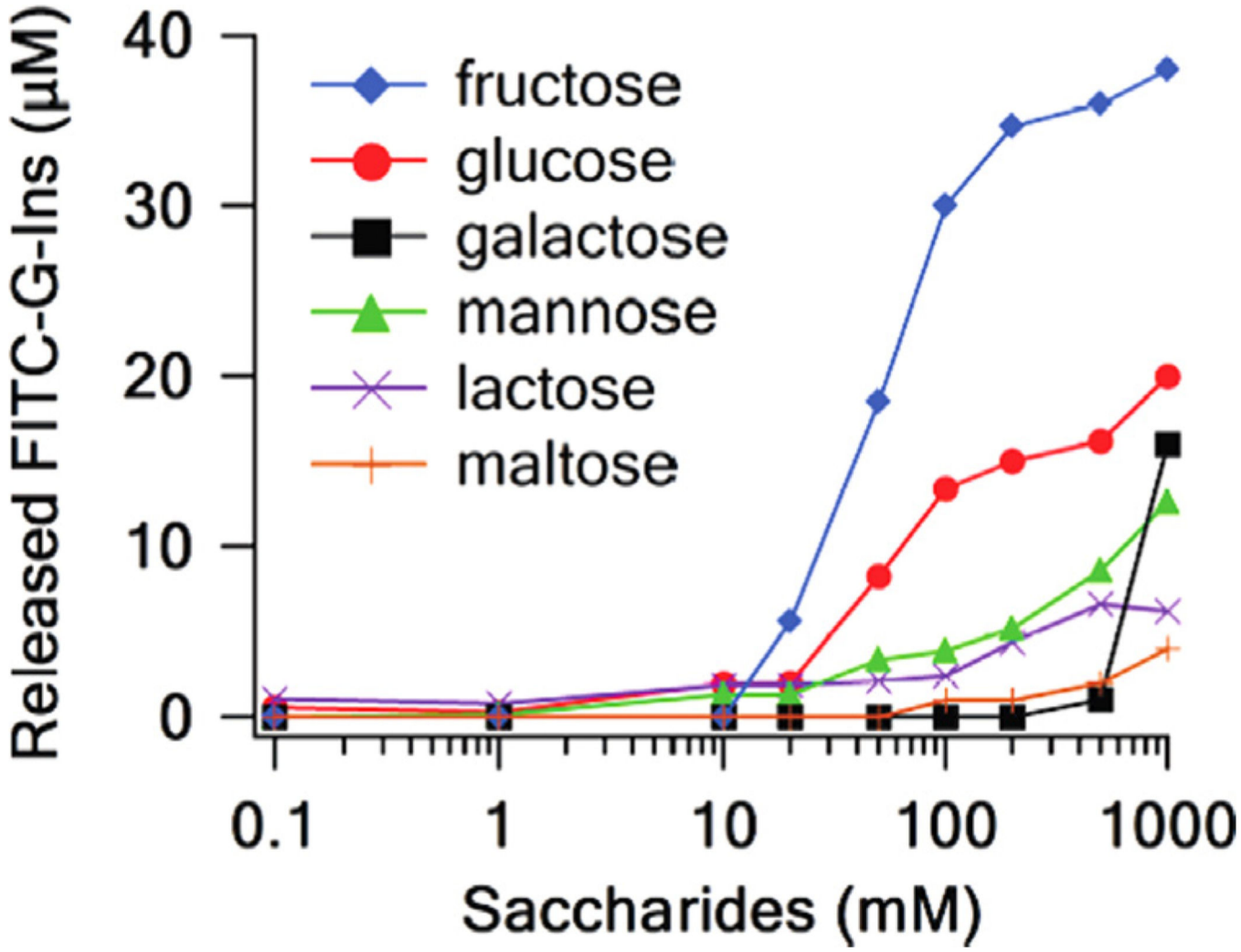

Fig. 23.

Release of FITC linked gluconic acid-insulin from mesoporous silica nanoparticles in the presence of various saccharides at pH 7.4 [119]. The gluconic acid-insulin cap is preferentially sensitive to fructose and glucose compared to other saccharides.

NIH-PA Author Manuscript
NIH-PA Author Manuscript
NIH-PA Author Manuscript

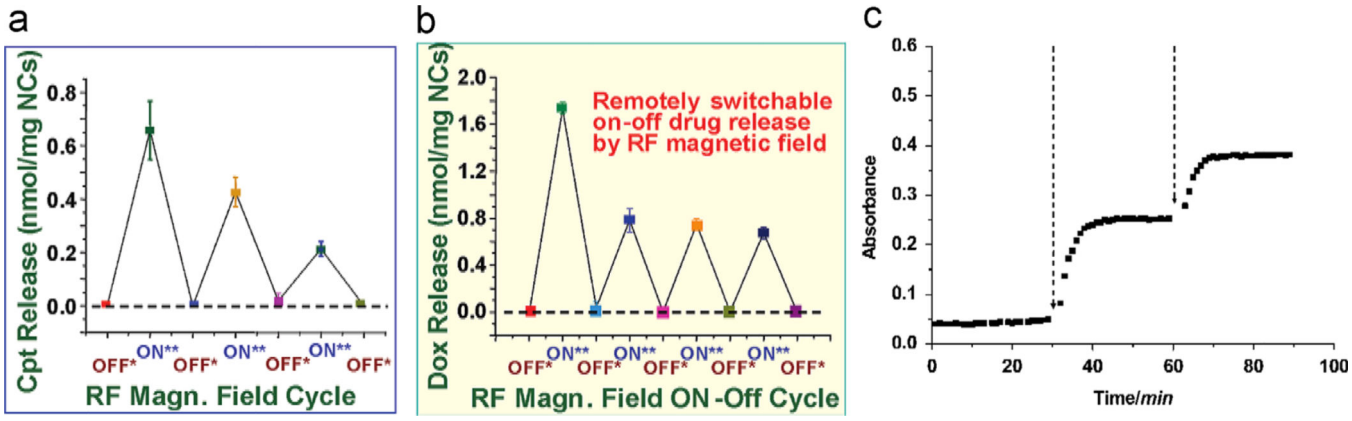

Fig. 24.

Externally triggered payload release from various silica nanoparticles [121]: (a) camptothecin release from SPION core–silica nanoparticles triggered by alternating magnetic field. For drag release, the AMF was “on” for 10 s and “off for 5 min. (b) Doxorubicin release from SPION core–silica nanoparticles triggered by RF magnetic field. When the AMF is turned off, there is no drug release. (c) Pulsatile payload (safranine O) release from Au nanoparticle capped mesoporous silica nanoparticles by 1064 nm laser excitation [123]. 5 pulses at 4.3 ns/pulse created a burst release which lasted several minutes after which more payload could be released with subsequent pulsing.

NIH-PA Author Manuscript

NIH-PA Author Manuscript

NIH-PA Author Manuscript

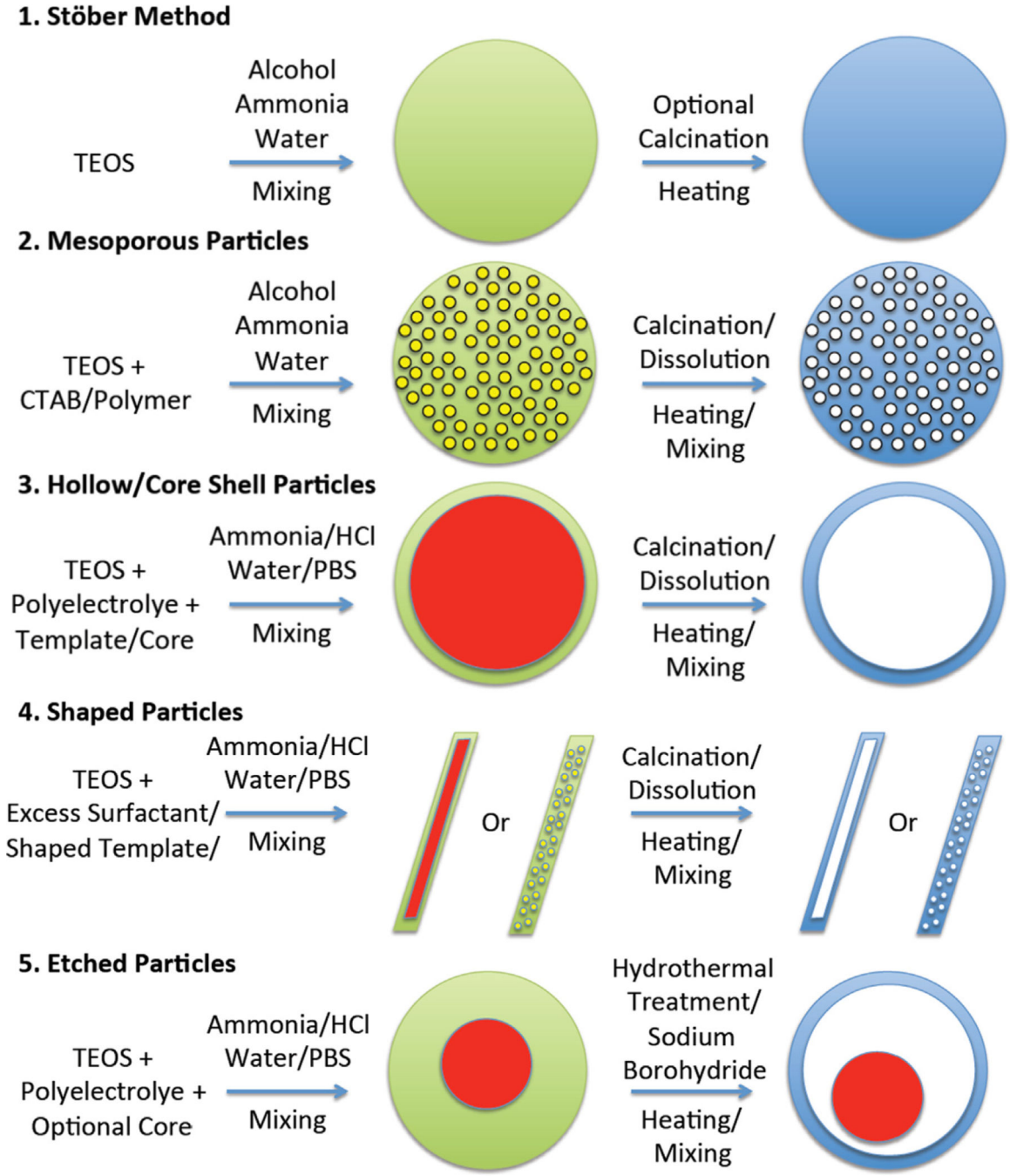

Scheme 1.
Common techniques in silica nanoparticle synthesis.